Advanced Course and Workshop on Blood Flow
BF 2005 – (pp.163–203) – Warsaw, 2005.

Heart Valves: Modelling Experiments

Giovanni Paolo Romano

Department of Mechanics and Aeronautics
Via Eudossiana 18, 00184 Roma, Italy
romano@dma.ing.uniroma1.it

Experimental results on the flow fields close to prosthetic heart valves measured by means of Particle Image Velocimetry (PIV) are reported. The attention is also focused on the different mock-loops employed to simulate the whole systemic circulation. Four experiments are reported: a pulsed jet with focusing onto the forcing mechanism simulation; a left ventricle with mitral and aortic prosthetic valves; two different mock-loops for aortic valves testing. The obtained results indicate that PIV can give results useful for biomedical evaluations not only in terms of mean field but also for higher-order statistics, i.e. in respect to the evaluation of damages on blood cells.

Key words: *Heart valves, PIV, fluid-mechanics*

1. Introduction on Heart Valve Flows

In this paper, experiments on artificial heart valves and on the way in which these can be simulated by an artificial apparatus are considered. The relevance of these experiments is multiple: from the scientific point of view, there are several complex fluid-mechanics phenomena which take part close to heart valves and are still unclear; from the social point of view, a proper characterisation of implantable prosthetic heart valves is required to save patients from critical health conditions; from the technological point of view, biomedical devices involve advanced solution which must be investigated by comparable advanced measurement and data analysis techniques. To attain these aims, a strict coupling between different approaches must be considered; numerical and experimental methods, experimental investigations in physiological ("in vivo") and in simulated ("in vitro") conditions, agreement on testing conditions and procedures.

In this section, the physiological behaviour of the heart and the working conditions of heart valves are summarised. In Sec. 2, the requirements for proper "in vitro" testing of artificial heart valves are considered. In Sec. 3, the experimental technique and the relevant measurement problems are briefly presented, whereas in Sections. 4 to 6 results on different mock-loops are reported. Remarks and future developments end the paper.

The operative conditions of the heart give origin to the cardiac cycle which is a complex sequence of events involving the heart itself and the whole organism. There are four heart valves involved in this cycle; in Fig. 1 the interior of the heart with the heart valves is shown. It is possible to notice the two atrial-ventricular (AV) valves (tricuspid and bicuspid or mitral) which separates right and left atrii from ventricles, and the two valves which allows blood to be pumped to lungs (pulmonary valve) and to the whole body through the aorta (aortic valve). As can be observed from the right part of the figure, there is a substantial difference among the tricuspid (and mitral) valves, having filamented leaflets (flap of tissue which constitute the valve), and the aortic (and pulmonary) valves which have a three leaflet configuration. The geometry of all valves is far from axial-symmetry; this is a very important point which must be considered in performing experiments on artificial valves.

The cardiac cycle is illustrated in Fig. 2, in which the non oxygenated blood (in blue) from the body enters into the right side of the heart (at the beginning the atrium and then the ventricle), while simultaneously the left part is filled with the oxygenated blood (in red) from the lungs. At this time, the AV valves are open while the other two are closed. After blood fills the

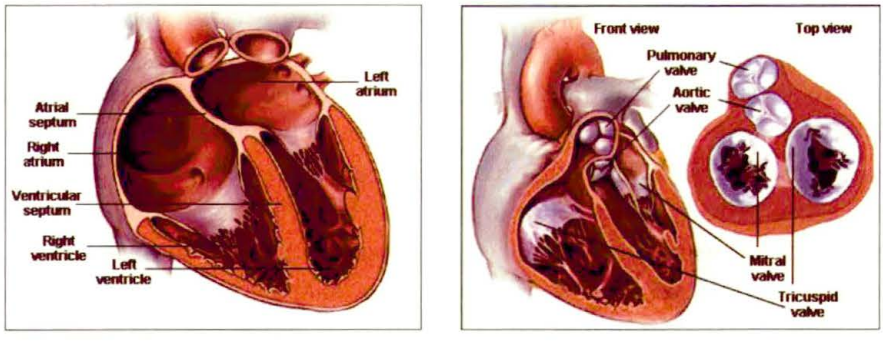

FIGURE 1. Internal division of the heart (on the left) and views of the four heart valves (on the right) (from GUIDANT, www.guidant.com).

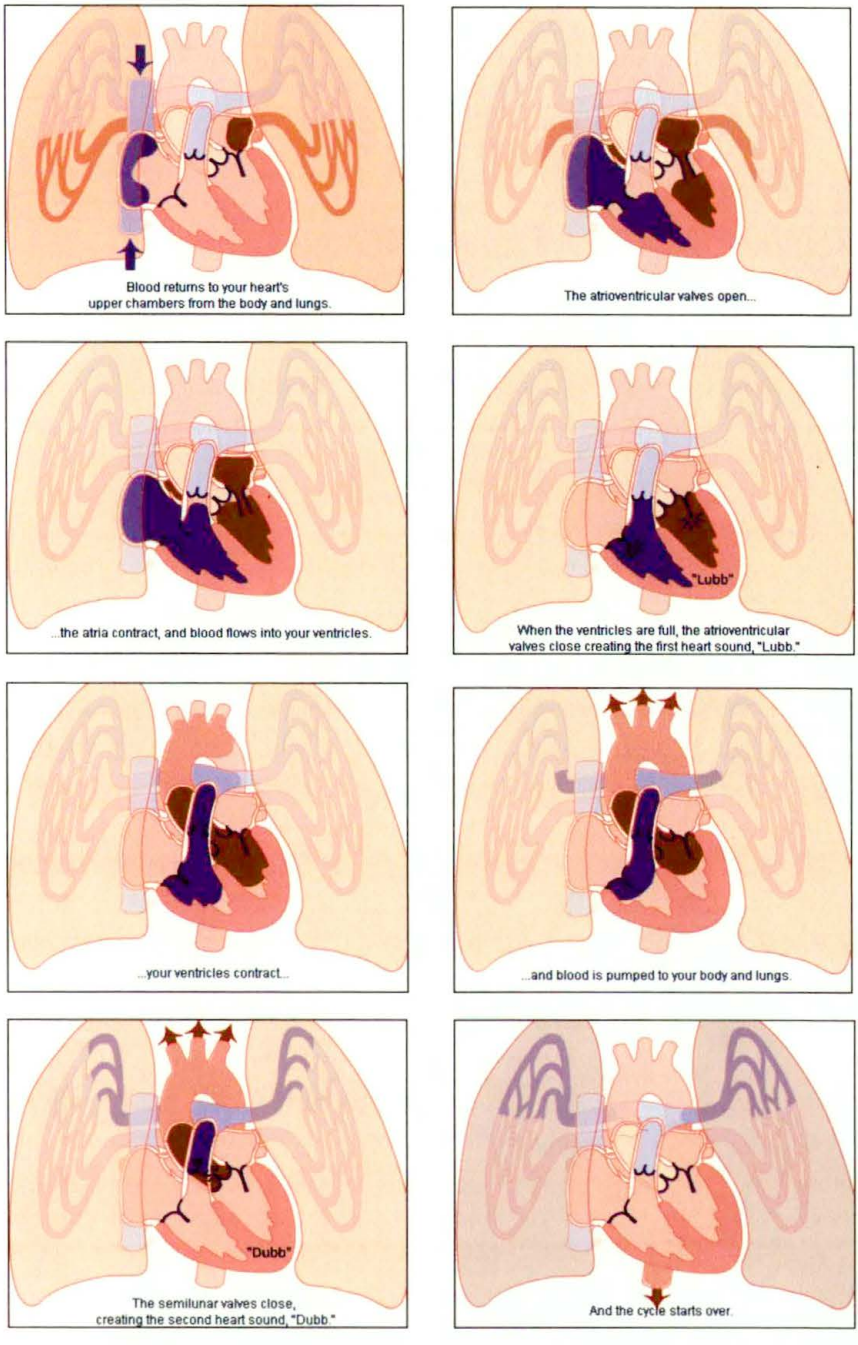

FIGURE 2. The cardiac cycle with oxygenated (red) and non oxygenated (blue) blood flowing into and from the heart (from GUIDANT, `www.guidant.com`).

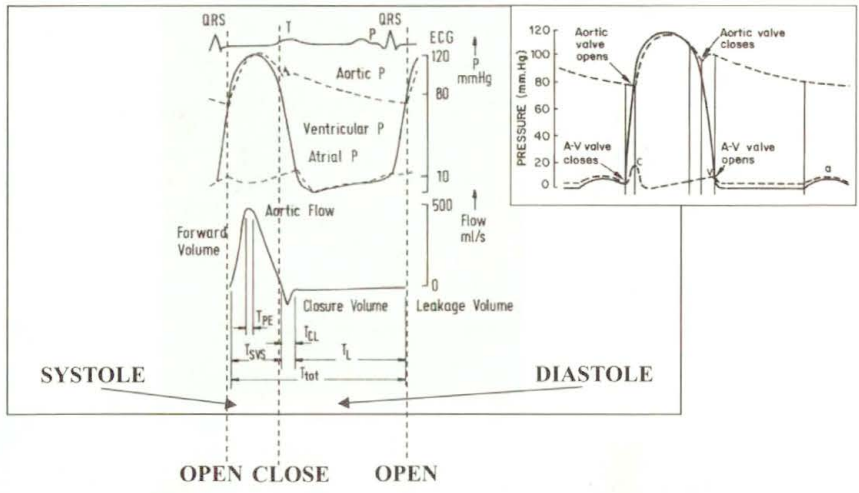

FIGURE 3. Behaviour of ECG signal, ventricular and aortic pressure (with expanded detail) and aortic flow rate during the cardiac cycle (from [1] www.engnetbase.com).

ventricles, the AV valves close and the other two open (due to the pressure difference between the ventricle and the regions downstream the valves themselves): oxygenated blood flows into the aorta, while non-oxygenated blood is directed towards the lungs. Then, the valves close and the cycle can start again.

As already written and as reported in Fig. 3, this cycle is controlled by the pressure difference among atrium and ventricle and the pressure difference among ventricle and aortic root; roughly speaking, the part of the cycle in which the atrial pressure overcomes the ventricular one is called diastole (AV valves are open), while the part in which the ventricular pressure is larger than the aortic pressure is called systole (the aortic valve opens). In the figure the echo cardio-graphic (ECG) trace and the corresponding aortic flow rate are also reported. The whole cycle gives rise to a strong unsteady, almost periodic (not sinusoidal) behaviour of the considered quantities (pressures, flow rates, ECG signals) which must be taken into account in simulating experimentally heart flow conditions.

The blood which is sent to the body is flowing into a complex system with smaller and smaller vessels (arteries and veins) which ended with arterioles and capillaries as schematically given in Fig. 4. This complex system (which has many similarities with complex hydraulics distributions systems or nets) has three main effects to be considered in experiments on heart valves:

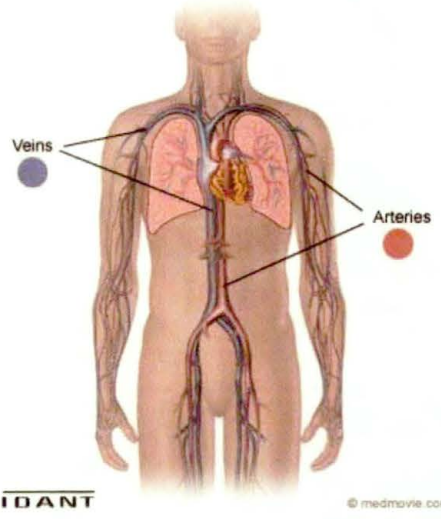

FIGURE 4. A simplified schematic of the blood circulation (from GUIDANT, www.guidant.com)

- the resistance to the flow due to the whole system (vascular resistance);
- the deformation of the wall of large arteries (arterial elasticity);
- the acceleration and deceleration of the blood into the vessels due to the cardiac cycle (arterial inertance).

These effects must be also taken in account for a proper experimental simulation of the heart working conditions.

Returning to the problem of the artificial heart valves, it must be considered that not only they have to resemble, as much as possible, the geometry of the problem, but also the flow induced phenomena. In particular, in Fig. 5 it is shown how some of the existent artificial aortic valves can alter the physiological behaviour of the flow; this will results in blood stagnation or recirculation which can generate thrombus and hemolysis, in energy losses through the valve in addition to bio-compatibility problems. Consider for example the cage-ball or the tilting disk flows in comparison to the natural normal case. This is why the recent advances in the field are towards bileaflet or even trileaflet valves which are more strictly related to the physiological case. The presence of the Valsalva sinuses (the cavities which incorporate the leaflets when opened in the natural case) also make the situation more complex in the artificial case (artificial leaflet do not open in the sinuses).

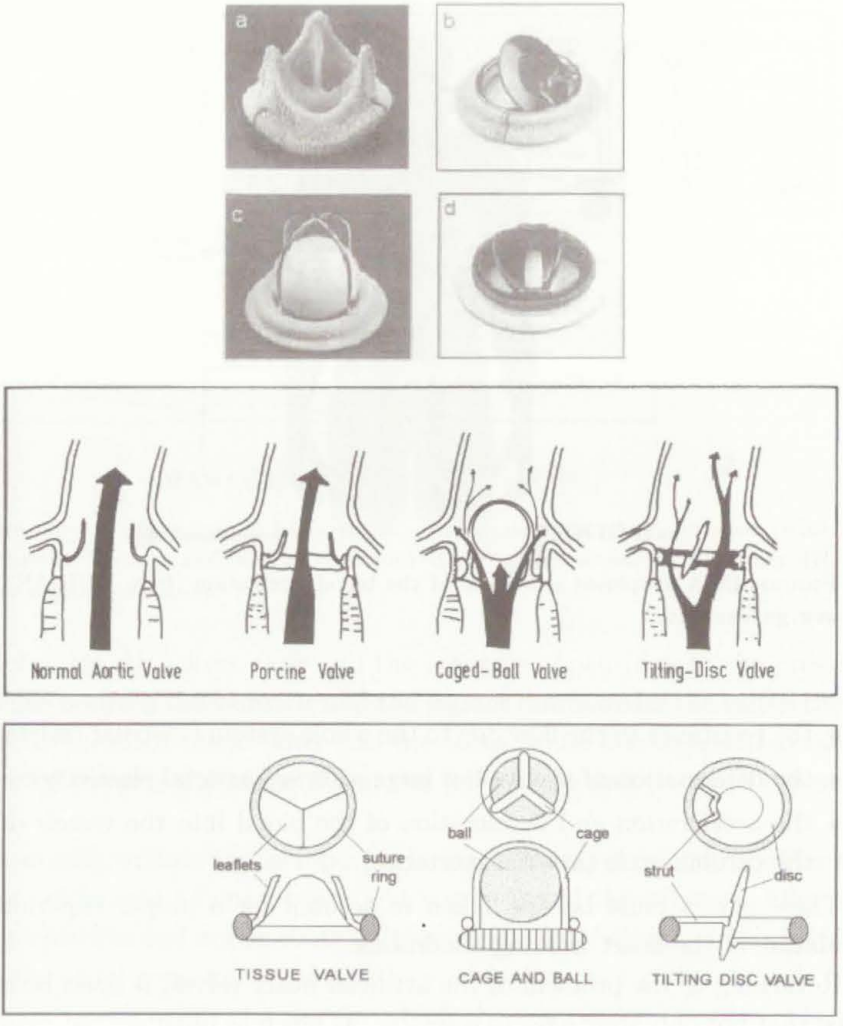

FIGURE 5. Different artificial aortic valves: photographs before implantation (at the top) and schematic of the flow behaviour after implantation (at the bottom) (from [1] www.engnetbase.com).

2. Artificial Simulation of the Systemic Circulation: Pulse Duplicators

Summarising the previous requirements, to mimic physiological flow conditions close to heart valves by means of a flow (hydraulic) circuit it is necessary to:

- simulate the unsteady cardiac cycle, in terms of beat frequency and stroke volumes, with proper forcing;
- simulate the blood pressures at several positions of the simulating circuit by proper set-up of the circuit itself;
- simulate the physical properties of the blood (*i.e.* density and viscosity) with a fluid which is effective to perform measurements with available techniques;
- simulate the vascular resistance with proper circuit elements (resistances);
- simulate the arterial elasticity with proper circuit elements (compliance and reservoirs);
- simulate the arterial inertance with proper circuit elements (inductance);
- simulate the complex geometry of the heart and of the initial part of the aorta with proper models;
- perform correct statistical analysis which takes into accounts the peculiarities of the considered signals and fields.

The previous requirements (need for resistance, compliance and inductance) frequently lead to the so called electrical analogy to account for the similarity among the two cases [5, 6].

These requirements hardly can be satisfied simultaneously. Historically, the first systems aiming to simulate the systemic circulation (also called pulse duplicators) do not consider the unsteady nature of the considered flow field. In Fig. 6, the pulse duplicator developed at Helmholtz Institute in Aachen by Reul *et al.* [2, 3] is shown. It consists of the aortic valve and root, fluid resistance and reservoir and forcing steady pump. The valve is mounted in a horizontal (non physiological) position. This apparatus was mainly used for visualisations and preliminary investigations.

Rather early the first unsteady pulse duplicators were developed; in Fig. 7, the one from the same Institute is shown consisting of atrial-ventricular models, aortic root model, compliances, resistances and inductances with unsteady adjustable forcing. The aortic and mitral valves are mounted in the vertical (physiologically correct) position. This system is very complete but also quite difficult to control. Some control parameters and velocity field results obtained with this mock-loop will be given in Sec. 6.2.

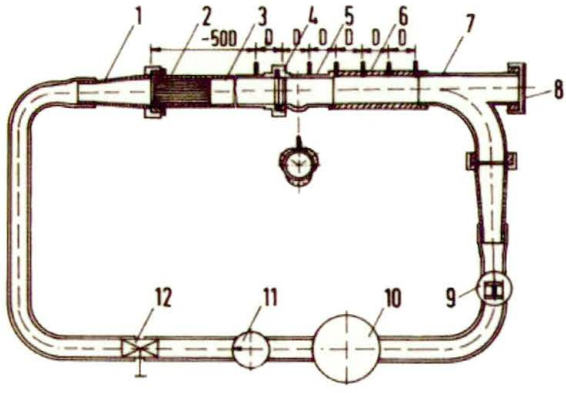

FIGURE 6. The Helmholtz Institute Aachen steady flow pulse duplicator (from [1] and [2]). (1) Flow inlet diffuser, (2) honeybomb, (3) inlet tube, (4) heart valve mounting ring, (5) model aortic root, (6) downstream measuring system, (7) bifurcation with optical observation window, (8) viewport allowing observation and recording of valve opening characteristics, (9) rotameter, (10) fluid reservoir, (11) centrifugal pump, (12) throttle valve.

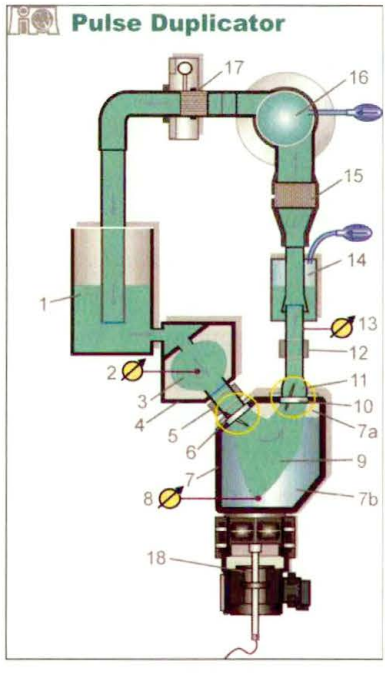

FIGURE 7. The recent Helmholtz Institute Aachen unsteady flow pulse duplicator (from [3]).

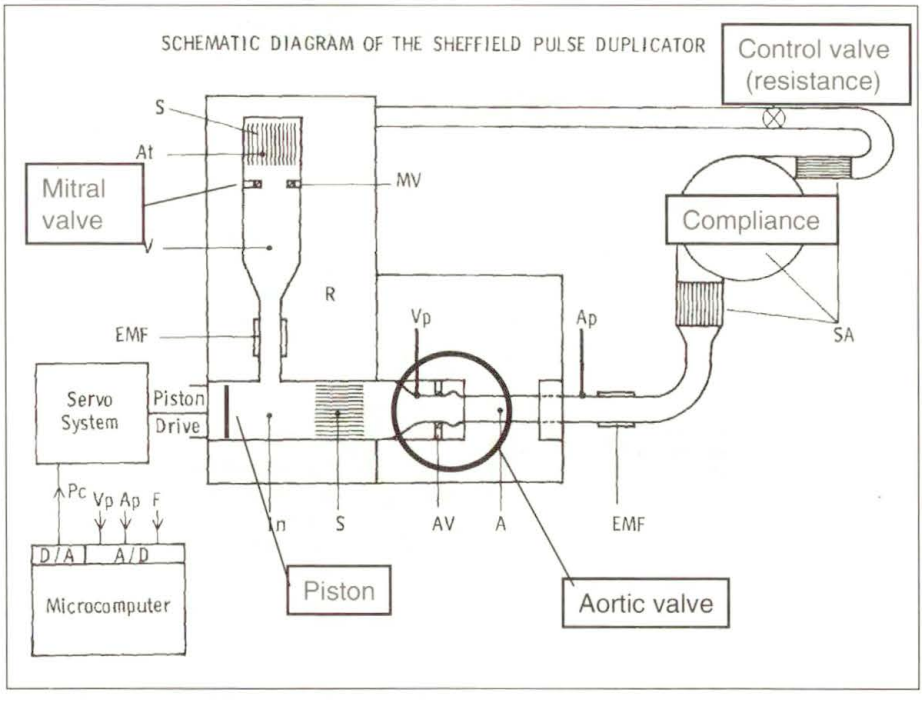

FIGURE 8. The Sheffield University unsteady flow pulse duplicator (from [4]).

In Fig. 8, the mock-loop developed at the University of Sheffield is shown; it is quite similar to the previous one except for the horizontal placement of the valve, the absence of ventricle with geometric similarity and the use of a rotating rather than linear motor. Some control parameters and velocity field results obtained with this mock-loop (namely the one at Istituto Superiore di Sanita' (ISS) in Italy) will be given in Sec. 6.1.

Commercial mock-loop started to be developed; an example is in Fig. 9, in which the Vivitro system with simulated left atrium and ventricle, compliances and resistances and forced by a waveform generator is shown. The aortic and mitral valves are placed in the vertical physiological position.

The standard measurement conditions to test heart valve flows are the following: cardiac output from 3 to 8 l/min, beat frequency equal to about 70 Hz, systolic duration equal to about 300 ms, mean aortic pressure equal to 100 mmHg and mean atrial pressure equal to about 10 mmHg. The working fluid is usually a water-glycerine mixture which ensure (at ambient temperature) matching with viscosity and density of blood and simultaneous transparency for measurement with optical methods.

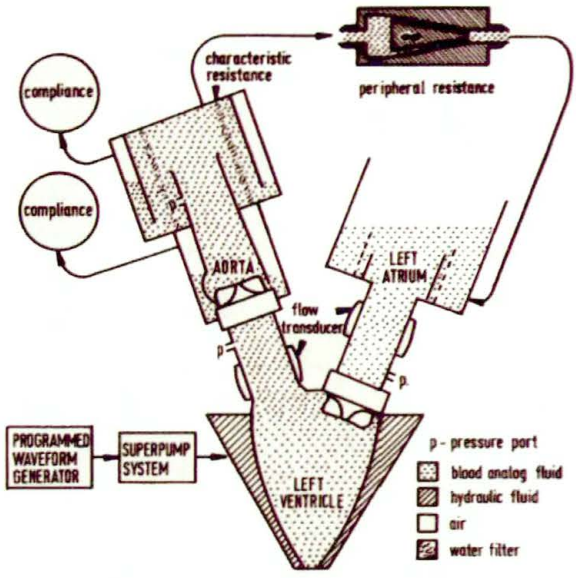

FIGURE 9. The commercial Vivitro unsteady flow left heart simulator (from [1] www.engnetbase.com).

3. The Experimental Technique: Particle Image Velocimetry (PIV)

It is not within the scope of this paper to describe the experimental techniques used in this investigation which are under the name of Particle Image Velocimetry (PIV). The reader is referred to [14, 15] and references therein for details. Here, only the main principles and specific problems for the considered investigation are reported.

In Fig. 10, a schematic of PIV is given: the flow is seeded with proper tracer particles (seeding) which have to follow the flow as much as possible. Providing that the test section is transparent, particles are illuminated by a strong light source (usually but not necessarily a laser). Images of the flow are taken by a videocamera which can be synchronised with the laser if light pulses are used or with a high rate framing in the case of continuous illumination (High-Speed PIV). Images contain positions of framed particles at two or several instants; by determining the distance between positions in consecutive frames it is possible to obtain the velocity of the particles themselves (the time interval between laser pulses or camera frames is known). To perform the displacement determination, dedicated software have been developed by many universities and producers; cross-correlation functions allow

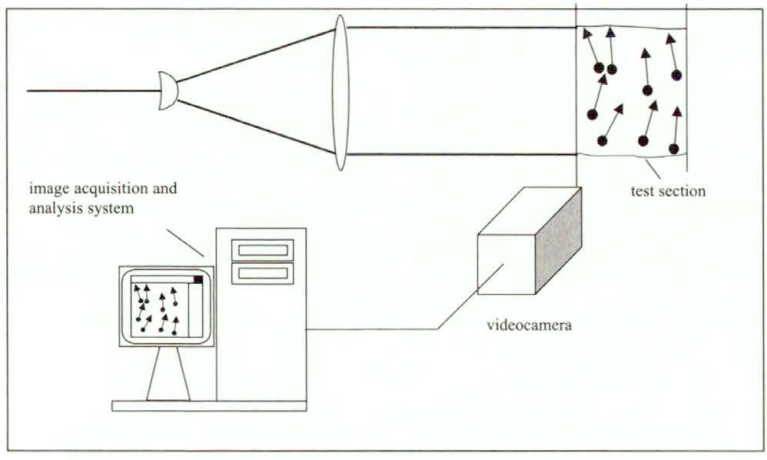

FIGURE 10. Schematic of a PIV system.

to derive the displacement of a group of particle statistically (proper PIV), while single particle displacements can be derived by tracking the particle along their trajectories (Particle Tracking Velocimetry, PTV).

The PIV technique is optical, non intrusive (except for the tracer particles), is linear without need for calibration and give two- or three-dimensional (Stereo-PIV) velocity fields. In the context of measurements in small vessels for biomedical applications, the following points must be considered with care:

- image distortions due to the curved geometry of the vessels;
- light reflections from the background and from the walls of the vessels.

In Fig. 11, an example of the former distortion at the aortic root is given; it is clear how the curved geometry makes distorted the grid placed inside the vessel (made by glass blown). To avoid this, in the second part of the figure, the inner and outer part of the glass blown aorta have been filled with a water-glycerine mixture which ensures a much better index matching.

In Fig. 12, the second problem is considered; in the first figure the aortic root field (valve at the top) shows many reflections from the walls and also internal to the test section (due to the curvature of the section). In the second part of the figure, the subtraction of the minimum intensity in each pixel, evaluated over a sample of 50 images of the flowing particles, allows to eliminate almost all reflections. This helps a lot in determining the particle displacements both with PIV and PTV. In the third part of the figure, an

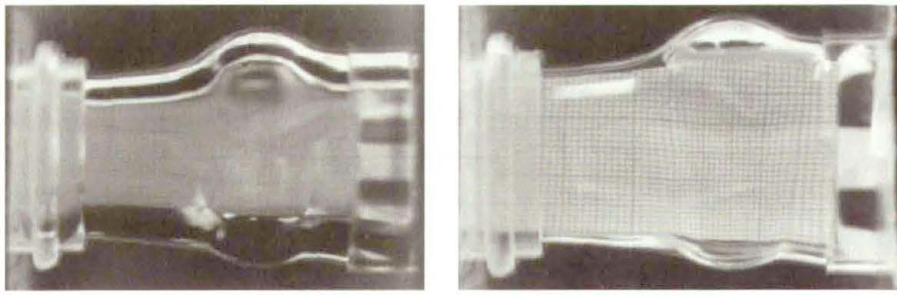

Empty root Root with glycerine

FIGURE 11. Image distortion due to glass blown aortic root geometry (left) and index-matching correction with water-glycerine mixture (right) (from [] www.engnetbase.com).

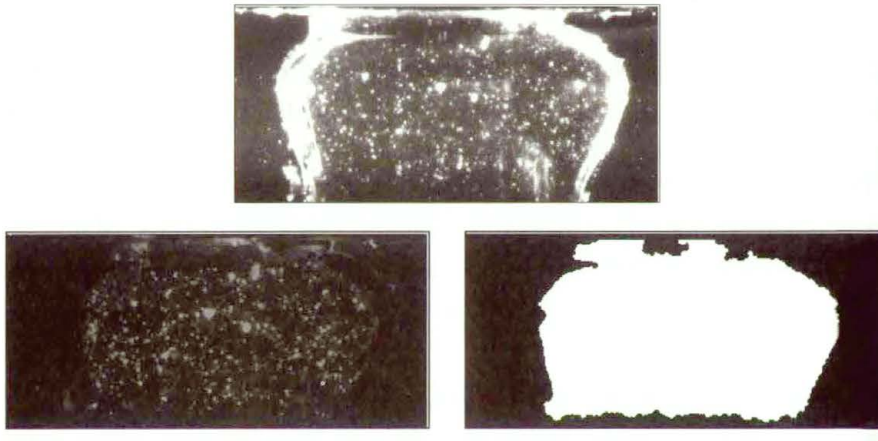

FIGURE 12. An instantaneous image of tracer particles in the aortic root of the Sheffield type pulse duplicator at ISS (at the top), image after background (minimum intensity) subtraction (at the bottom left) and automatic mask image (at the bottom right).

automatic mask has been derived for the considered field; this procedure allows to compute the flow field only where the mask is white (test section) and to avoid the computation outside the interest field (black region).

Image pre-processing (as well as image post-processing) as that depicted previously, can give large improvement in the determination of velocity fields with PIV related techniques.

4. Investigation on a Pulsed Jet

The first experimental results concern with a quite simple flow condition, a pulsed jet from an orifice; this set-up has been considered to investigate the effect of the forcing signal shape and amplitude on the resulting flow field.

In Fig. 13, the experimental set-up used for this experiment is shown; it consists of a piston driven by a synchronous linear programmable motor (arbitrary shape, amplitude and frequency) which forces the flow into an orifice; the hydraulic circuit is completed by valves to reduce regurgitation as much as possible. The peak Reynolds number is equal to 2.5×10^4; conventional cross-correlation PIV has been used. Details are given in [9, 12, 13].

In Fig. 14 the used forcing signal displacements and velocities are given; they are sinusoidal, exponential, ramp1 (faster) and ramp2 (slower). Each imposed signal consists of 1000 data points with feedback control (digital optical encoder) ensuring 0.1% deviation from the imposed signal. These signals have been selected to reproduce flow rate data which can occur in simulating heart valve flows.

An overview of the flow field downstream the orifice is given in Fig. 15; each of the plots is obtained as phase averaging (averaging at the same position of the piston) of 50 instantaneous fields. The vector and vorticity fields show a vortex ring (on the plane only two counter rotating vortices) travels from right to left. It is followed by a trailing jet, i.e. two shear layers of distributed vorticity.

Concerning averages and statistics evaluation, it is important to point

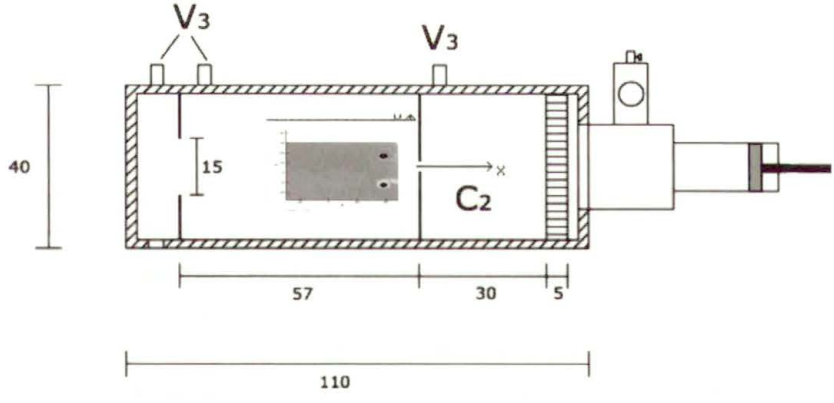

FIGURE 13. The experimental set-up for the pulsed jet configuration.

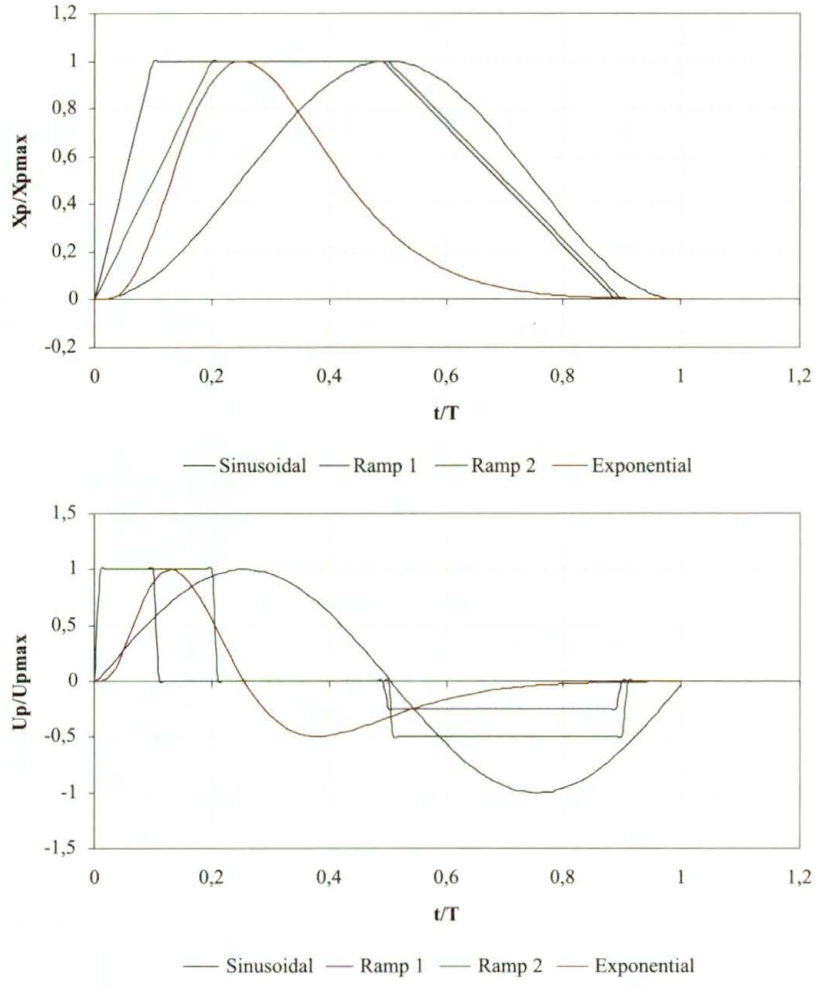

FIGURE 14. The forcing signals for the motor: displacement (at the top) and velocity (at the bottom).

out two aspects: first of all, phase averaging is strictly required to capture the correct velocity fields in pulsating flow conditions. Usual time averaging would give non useful results. This means that the motion of the driving system must be coupled with the image acquisition system. Secondly, the number of images required for statistics could be crucial.

To this end, in Fig. 16, the vertical (transverse) mean velocity is given for a number of phase averaged images from 10 to 1000; the overall field is independent on the number of employed samples for statistics.

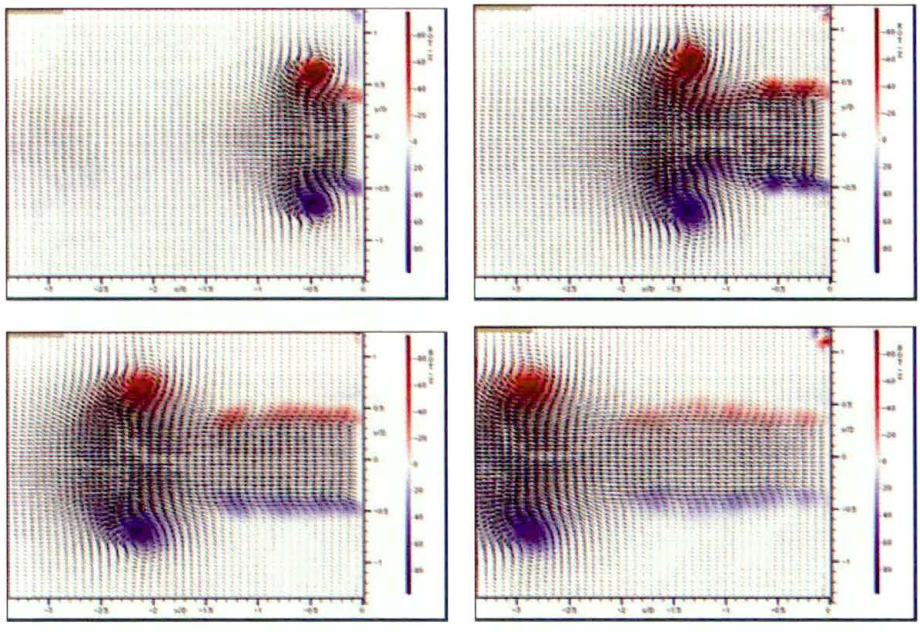

FIGURE 15. Overview of the phase averaged velocity vector and vorticity fields at four different phases for the sinusoidal forcing (flow rate equal to 70 ml). Mean flow from the right.

This is also confirmed by Fig. 17, where the profiles of mean axial velocity and vorticity along the dotted line of Fig. 16 are given for different sample number. They are practically coincident. This result concerns with first-order statistics (mean values). When second-order is considered, the situation changes; in Fig. 18, the RMS horizontal velocity is given for the same sample numbers as before; in this case, while in the low fluctuation regions (in blue) a rather low number of samples is sufficient (50–100), in the high fluctuation regions (in green and red) the required number of samples for statistical convergence is higher (500 or 1000). This statement is confirmed in Fig. 19, in which profiles of the RMS horizontal velocity and of Reynolds stresses are presented; especially the last quantity requires a high number of samples to converge statistically.

After establishing the required number of samples for statistical convergence, the analysis was focused onto the effect of the flow rate for the same forcing signal. In Fig. 20, three different flow rates are considered for the sinusoidal signal (50 ml, 70 ml, and 90 ml). The horizontal phase averaged

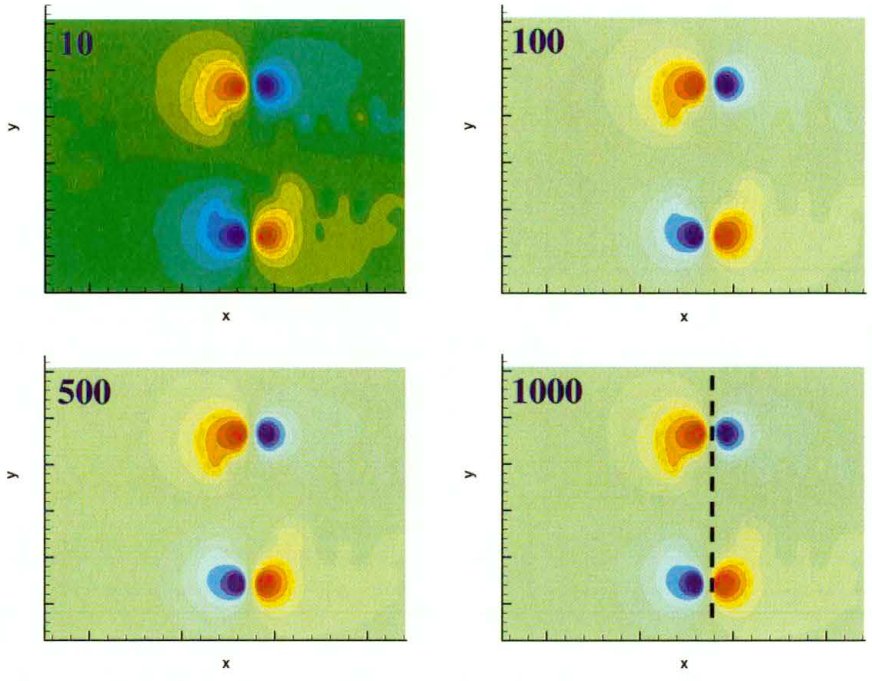

FIGURE 16. Statistical analysis on the phase averaged vertical velocity as a function of the number of samples used; sinusoidal forcing with flow rate equal to 70 ml.

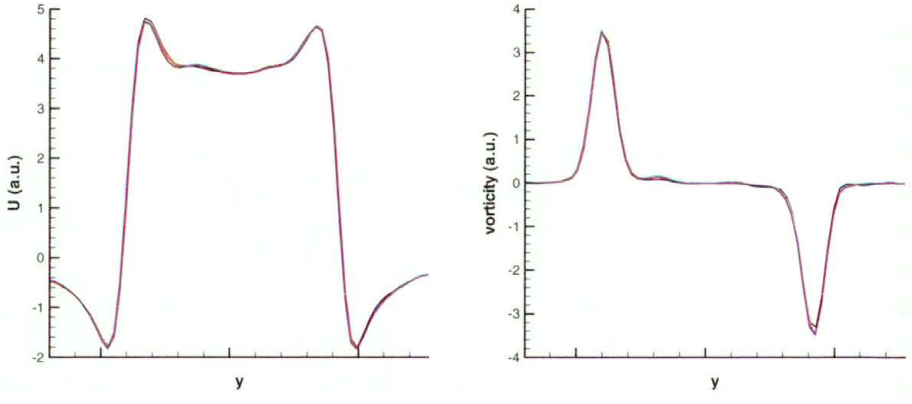

FIGURE 17. Statistical analysis on the phase averaged horizontal velocity (on the left) and vorticity (on the right) profiles as a function of the number of samples; sinusoidal forcing with flow rate 70 ml. Number of samples equal to 10 (black lines), 100 (red lines), 500 (green lines) and 1000 (blue lines).

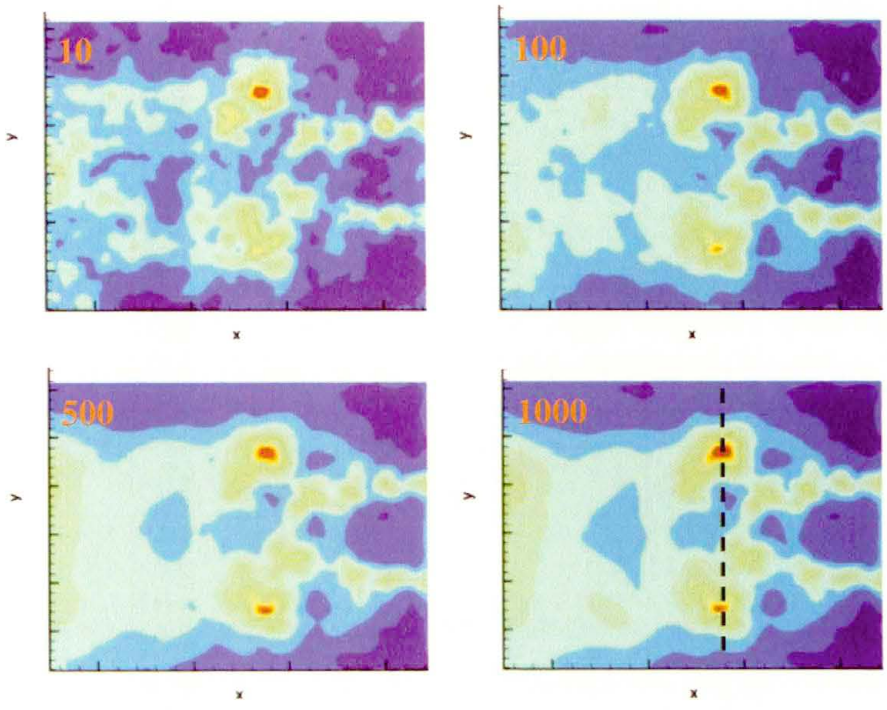

FIGURE 18. Statistical analysis on the phase averaged RMS horizontal velocity as a function of the number of samples used; sinusoidal forcing with flow rate equal to 70 ml.

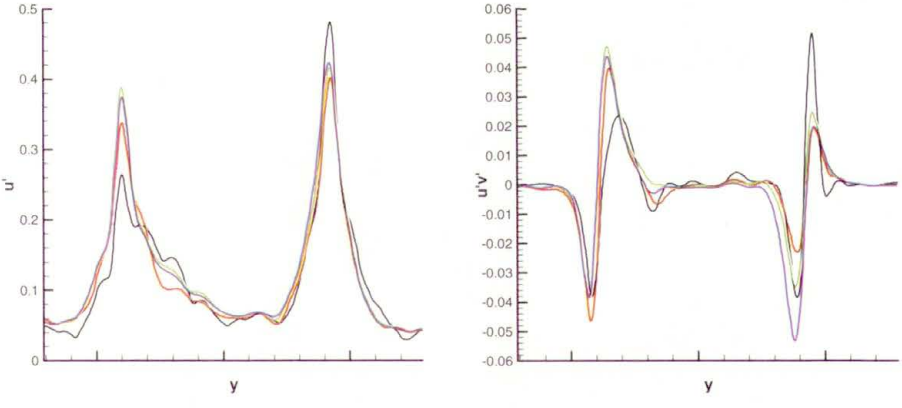

FIGURE 19. Statistical analysis on the phase averaged RMS horizontal velocity (on the left) and Reynolds stress (on the right) profiles as a function of the number of samples; sinusoidal forcing with flow rate 70 ml. Number of samples equal to 10 (black lines), 100 (red lines), 500 (green lines) and 1000 (blue lines).

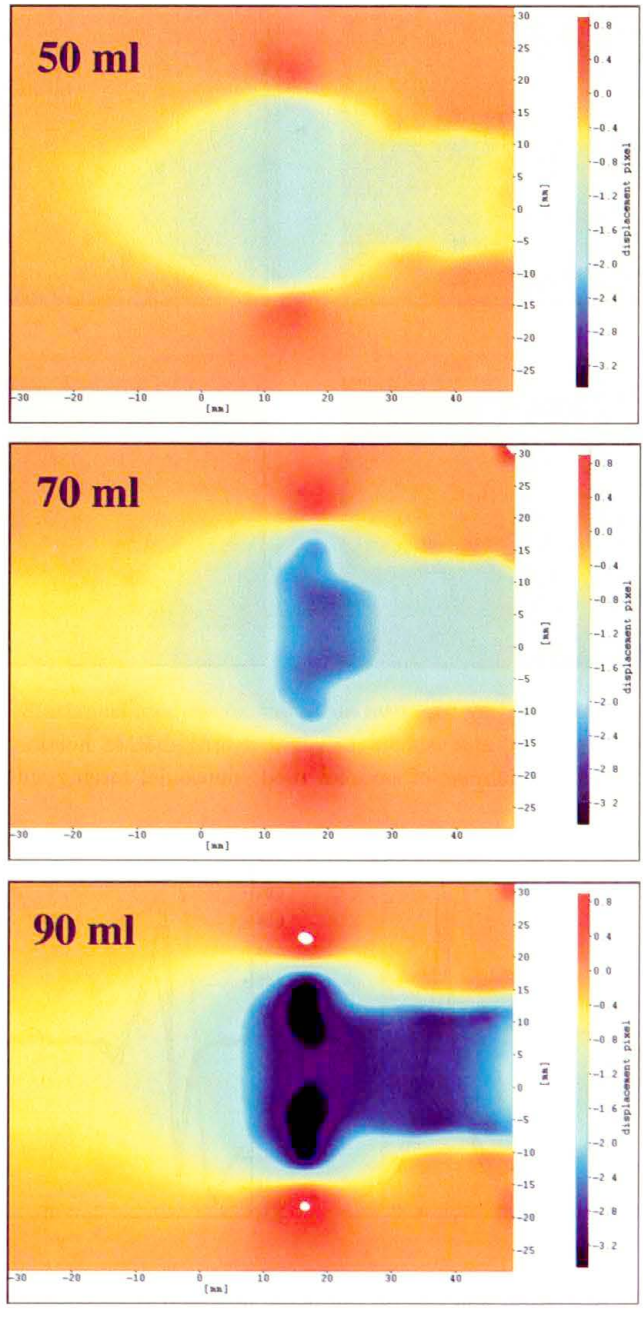

FIGURE 20. Phase averaged horizontal velocity component at different flow rates (same colorbar) at almost the same positions; sinusoidal forcing.

velocity shows two main effects: the intensity of the vortex ring of course increases as the flow rate (the same colorbar is used). Secondly, while for the 50 ml case the vortex ring is almost isolated, for the higher flow rates there is a connection with the trailing jet which follows the main ring.

The interaction between the two (vortex ring and trailing jet) is even better pointed out by the analysis of the second-order statistics; in Fig. 21, the RMS of the vertical velocity is given for the same data of Fig. 20. The two isolated counter rotating vortices are clearly identified for the 50 ml case, while the strong connection and interaction with the trailing jet is emphasised in the 70 ml and 90 ml conditions. This happens under the form of a continuous layer (70 ml) or of discrete vortical elements (90 ml). Similar results have been obtained for the other tested signals at the different flow rates. Thus, increasing the flow rate downstream of an orifice not only increases the intensity of the vortical structures but also change the way in which they interact with the neighbour fluid [16].

The other effect which is investigated is the one related to the shape of the driving signal (as reported in Fig. 14). The horizontal phase averaged velocity of the four tested signals is given in Fig. 22 at the same flow rate (70 ml); even in this case differences appear not only in the form of different intensities of the vortex ring (same colorbar used), but also in the form of different topology. In particular, the interaction with the trailing jet is through an almost continuous layer for the sinusoidal and slow ramp (ramp2) conditions, whereas distinct vortical structures are observed for the exponential and fast ramp (ramp1). This is because the latter have a more impulsive forcing (i.e. over a shorter time interval) to drive the piston in comparison to the former.

As shown in Fig. 23, the analysis of second-order statistics confirm these findings; the discrete vortical structures are clearly visible in the results of the exponential and the ramp1 (on a lower extent for the ramp2 also).

The results from the ramp1 also indicate a strong interaction among the primary vortex ring and that which can be called the secondary vortex ring; in the other phases the two exploit a precession one around the other. Thus, the effect of the signal shape, as for the flow rate, is also visible both on the intensity and on the shape and interaction of the created vortical structures.

Velocity profiles have been computed from the previous phase averaged velocity field; at the inlet, these profiles can be compared to investigate the birth of the vortex ring (all the relevance of this work in connection to heart valve application is strictly limited to the near orifice flow). In Fig. 24, the

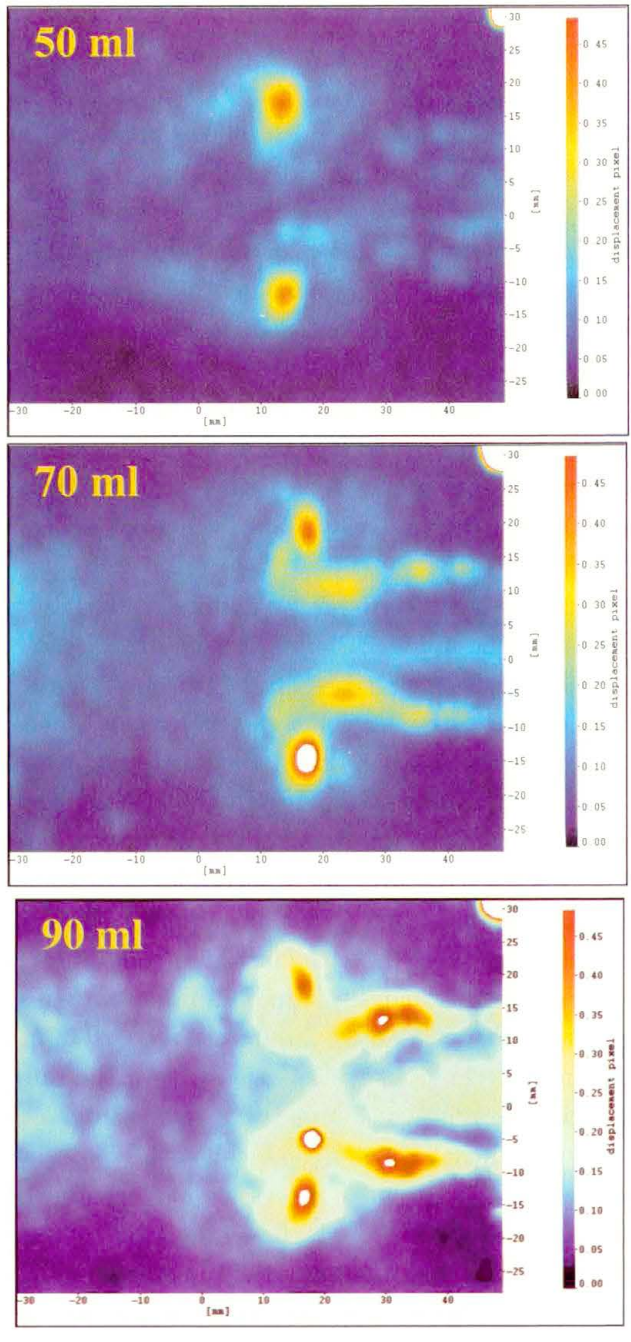

FIGURE 21. Phase averaged RMS vertical velocity component at different flow rates (same colorbar) at almost the same positions; sinusoidal forcing.

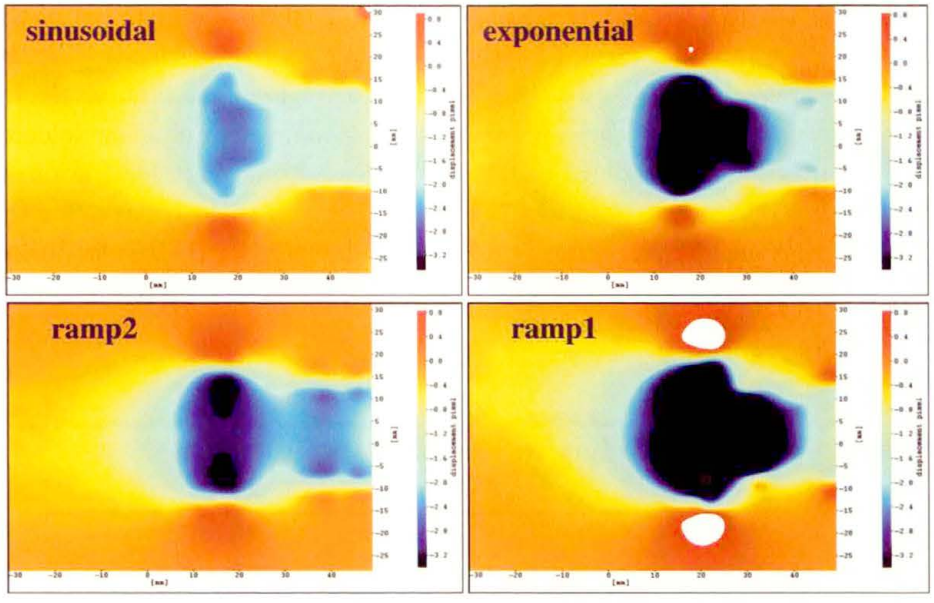

FIGURE 22. Phase averaged horizontal velocity component for different forcing signals (same colorbar) at almost the same positions; flow rate equal to 70 ml.

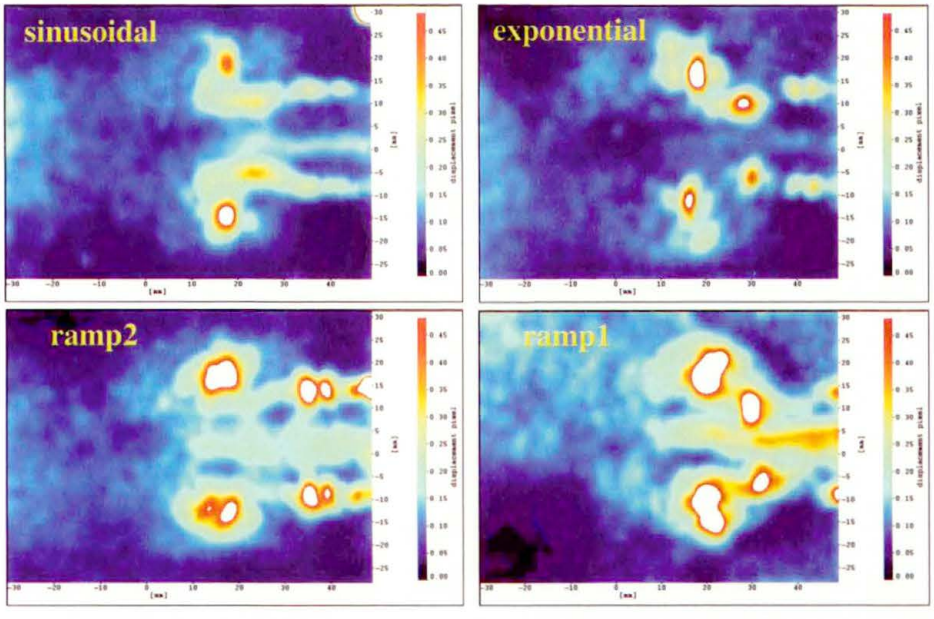

FIGURE 23. Phase averaged RMS vertical velocity component for different forcing signals (same colorbar) at almost the same positions; flow rate equal to 70 ml.

profiles for the four different tested signals are given. In the first part of the figure, the data are normalized by the maximum discharge velocity (*i.e.* the maximum horizontal velocity at the inlet) for the phase of maximum velocity (positive velocities) and normalized by the maximum regurgitation velocity (i.e. the maximum horizontal negative velocity at the inlet) for the phase of regurgitation (negative velocity). Even if there is a slight collapse for the curves during the discharge, there are strong differences for the results during regurgitation. In the second part of the figure, all data are non-dimensional

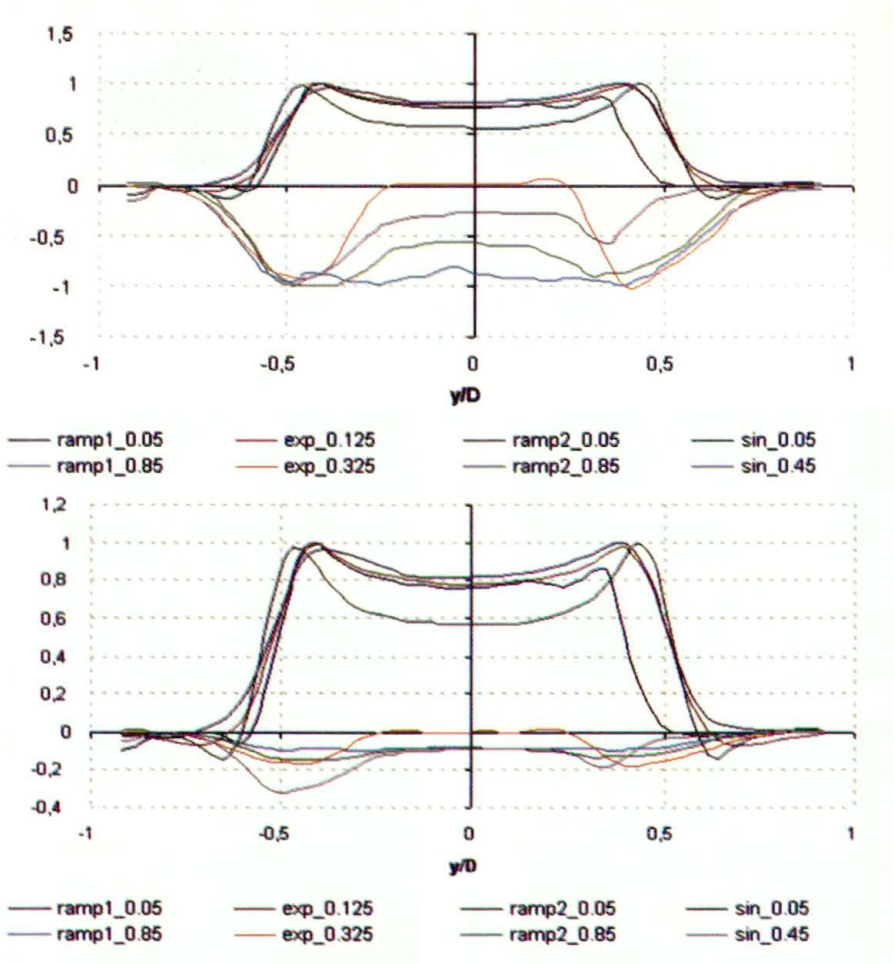

FIGURE 24. Phase averaged horizontal velocity component inlet profiles for different forcing signals; normalized by the maximum discharge and regurgitation velocities (at the top) and by the maximum discharge velocity (at the bottom); flow rate equal to 70 ml.

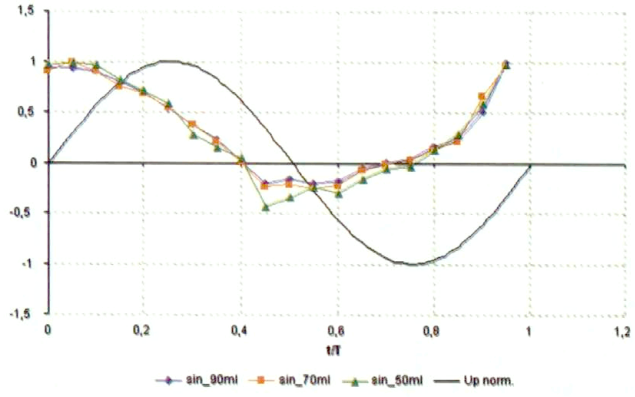

sinusoidal

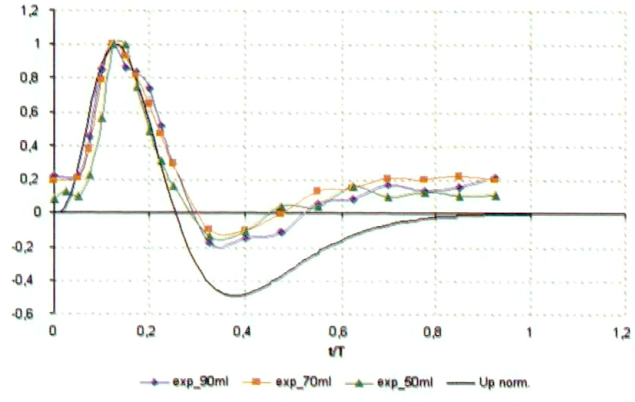

exponential

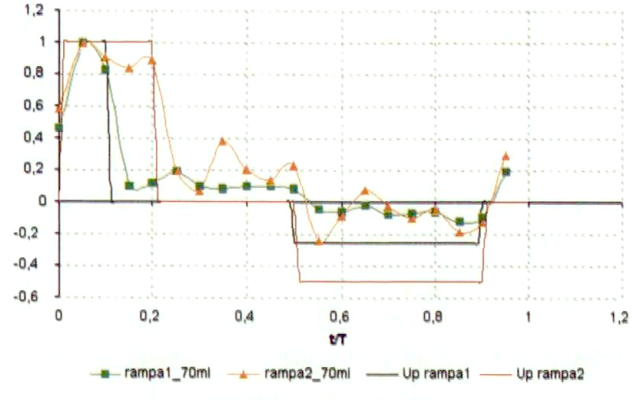

ramp1 and ramp2

FIGURE 25. Average inlet velocity measured by inlet velocity profiles of Fig. 24 (in different colours for different flow rates); comparison with given motor velocities in continuous black lines (from Fig. 14) for the different forcing signals.

by the maximum discharge velocity. Also in this case the collapse of the results is poor during discharge and regurgitation especially for the fast ramp case. Thus, this result confirms that there is not a simple scaling when considering different forcing signals for such a kind of flows; results obtained with a given forcing signal at a given flow rate hardly can be generalised to other conditions. For heart valve testing, this means that exact signals for flow rate and pressure must be used (*i.e.* the pulse duplicator must be tuned with particular care).

From the above inlet profiles, flow rate can be computed easily by integration; the results are given in Fig. 25 for the four signals tested at the different flow rate; in the figure the velocity imposed to the piston by the motor for each forcing signal is also given (as reported in Fig. 14).

For the exponential and the ramps the results are in good agreement with the imposed signals showing that the hydraulic circuit responds almost in phase with the piston movement; for the sinusoidal forcing, there is a phase shift indicating that the circuit replies with some delay to a more regular movement in comparison to the others. The shape of the signals show that the discharge phase is activated properly and that the discharge is attenuated although not completely avoided (in some sense this is an important result for applications of the circuit to heart valves due to the fact that some regurgitation is always present in prosthetic valves. There are not noticeable differences among the results obtained at different flow rates.

5. Simulation of Left Ventricle with Mitral and Aortic Valves

The second reported experiment concerns with a simulation of the left ventricle with mitral and aortic valves; in this experiment, the tilting disks valves have been used, while the ventricle is made by transparent, deformable silicone rubber. The experimental set-up is shown in Fig. 26; in the first part of the figure, the alignment of the laser and videocamera in respect to the left ventricle model (forced by a linear motor controlled by PC similar to the one described in Sec. 4) are presented. In the second part of the figure, the silicone rubber ventricle model is detailed; the open mitral valve at the top can be clearly noticed. When the piston moves, the ventricle has to adjust its volume accordingly. In the third part of the figure, the flow rate variation in time is given (the signal is based on physiological laws as those presented in Sec. 1); note that the diastole corresponds to the filling of the ventricle. Water is used as working fluid.

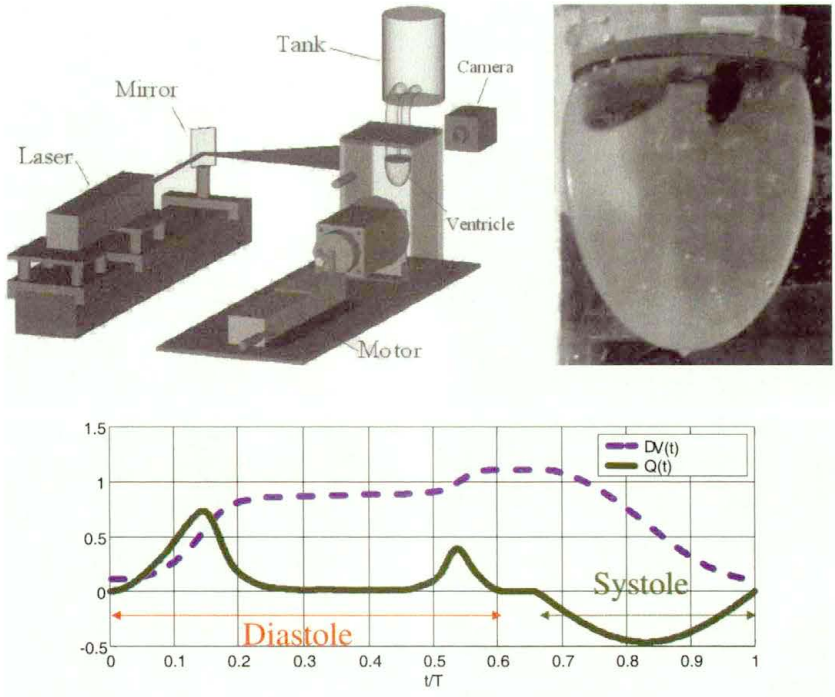

FIGURE 26. The experimental set-up for the left ventricle configuration (at the top) with details on the silicone rubber ventricle (at the centre) and on the flow rate in the cycle (at the bottom).

Images have been recorder by a high speed camera (up to 500 Hz at full resolution) and Particle Tracking Velocimetry was used to determine particle trajectories and velocities [17]. Further details on the experimental set-up and procedures are given in [8, 10, 11].

An overview of the flow behaviour is given in Fig. 27 where particle trajectories are depicted; at the opening of the mitral valve (first figure), the flow enters into the ventricle and due to the titling valve it takes the form of two adjacent jets forming vortex rings as in the previous experiments (Sec. 4).

During the diastole, these jets hit the wall of the ventricle at different positions (the left jet on the left part and the right jet on the right part) (second part of the figure); this interaction causes a flow along the ventricle wall which turns back towards the inlet forming several smaller vortical structures (third figure). When the mitral valve closes, the flow in the ventricle is almost at rest everywhere (fourth figure).

Phase averaged velocity are obtained from the particle trajectories; they are projected into a regular grid and shown in Fig. 28 together with the vor-

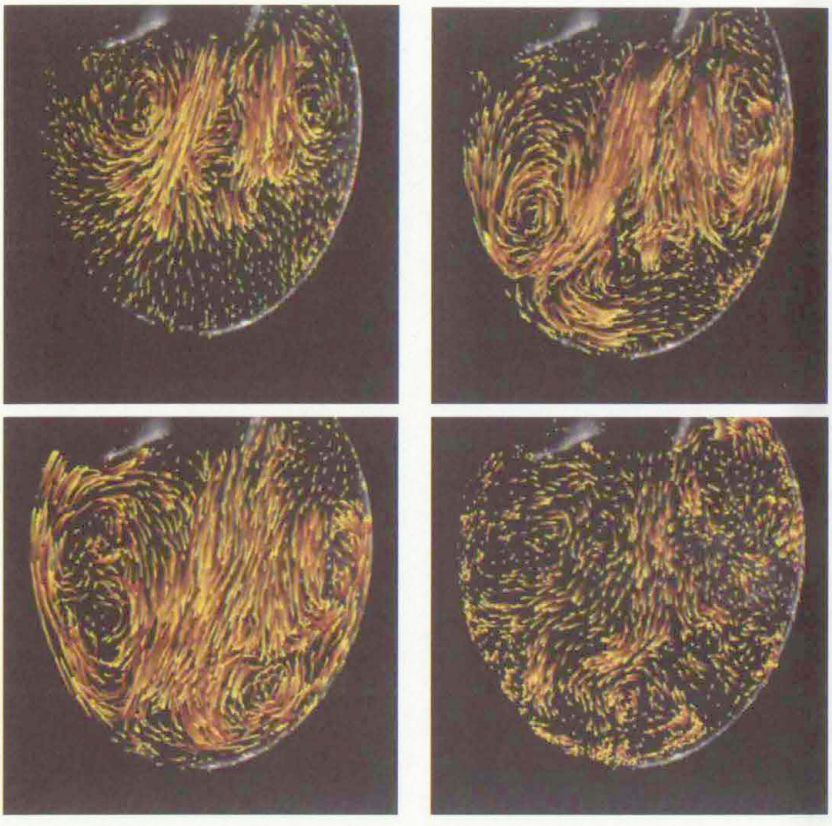

FIGURE 27. Particle trajectories at four phases of the cycle; mean flow from the top.

ticity; the phases are almost the same as those presented in Fig. 27 (indicated by red dots over the flow rate curve in each figure). Two opposite signs vorticity layer are obtained at the opening of the valve (first figure); this result is different from that of an isolated vortex ring and seems to be better described by two vortex rings connected to trailing jets (see Sec. 4).

In the second part of the figure, the two vortices are going to hit the ventricle walls but are still well defined; a layer of opposite sign vorticity is detached from the wall due to the induced velocity field by the stronger vortex ring (on the left). After the impact on the wall, layers of distributed vorticity return towards the inlet along the wall (third part of the figure); this is a clear effect due to confinement into the ventricle. The final figure does not correspond to the fourth of Fig. 27; it is obtained immediately after the second peak in the flow rate (so called A wave, while the first maximum is called

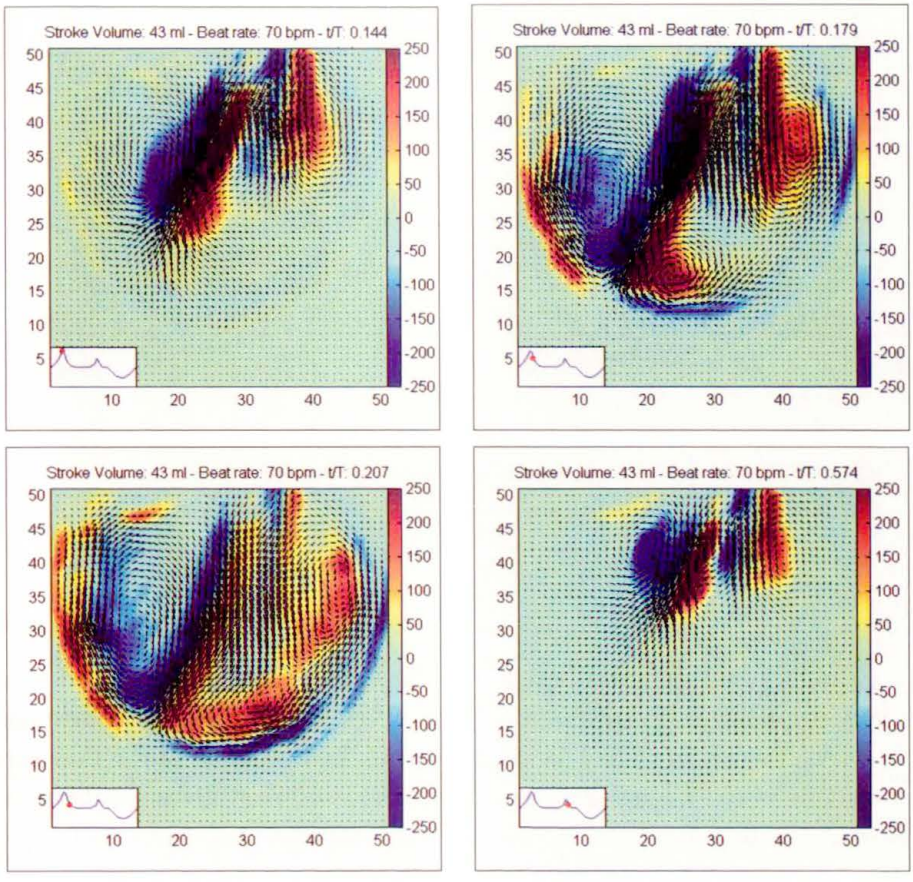

FIGURE 28. Phase averaged velocity vectors and vorticity contours at four phases of the cycle (indicated by the red dots).

E wave), when the mitral valve re-opens for a short interval. A new couple of jet is observed but the intensity is fairly smaller than before; they will dissipate before colliding on the ventricle wall. This presented measurements have been performed with an equivalent beat rate equal to 70 Hz and a flow rate equal to 3 l/min.

It is important to point out that frequencies have been rescaled to account for differences between the used fluid (water) and blood; Reynolds (equal to about 700) and Womersley (equal to about 19) numbers similarity is achieved.

Higher-order statistics is computed on these data; in Fig. 29, the turbulent kinetic energy (*i.e.* the sum of mean square fluctuating velocities on the measurement plane) non-dimensional by the average outlet velocity is given

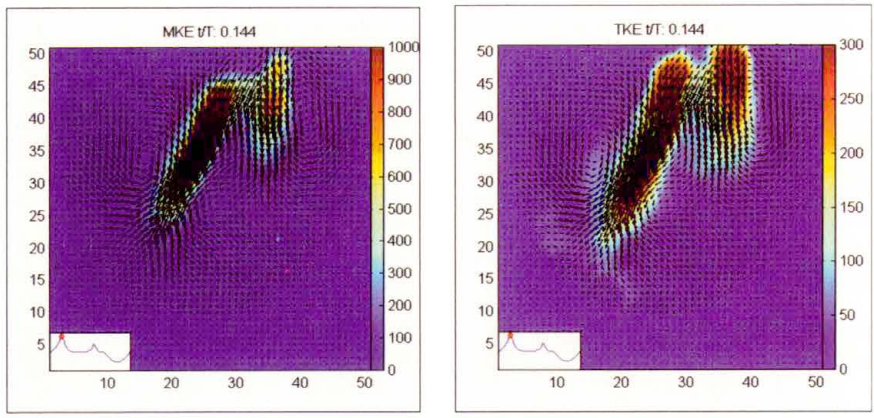

FIGURE 29. Phase averaged mean (on the left) and turbulent (on the right) kinetic energy at one phase of the cycle (indicated by the red dots).

(on the right part). It is compared with the sum of the phase averaged mean velocity components on the plane (i.e. the average kinetic energy) made non-dimensional as before. They are evaluated at the first peak of the flow rate, E wave). It is clear that the turbulent fluctuating part gives a substantial contribution in comparison to the average term (in the order of 30%), so that it cannot be neglected even at this quite small Reynolds number.

A comparison similar to the previous one has been performed on the viscous and turbulent shear stresses; they are obtained from the eigenvalues of the viscous and Reynolds stress tensors on the measurement plane (i.e. four components). The results obtained for the two, at the same phase as Fig. 29, are given in Fig. 30; in this case, the relevance of the turbulent contribution is much larger than before. There is almost a factor 100 between the viscous and turbulent contributions; this situation is quite common in blood flow investigations so that turbulent contributions to stress on blood cells are usually the largest.

The presented results concern with statistics obtained in time (or better in phase) at each point (Eulerian statistics); however, the PTV technique allows to derive also statistics along particle trajectories (Lagrangian statistics). Examples of results obtained with Lagrangian statistics are given in the next section; the reader is referred to [8, 10, 11] for other results on Lagrangian statistics obtained in the silicone ventricle model.

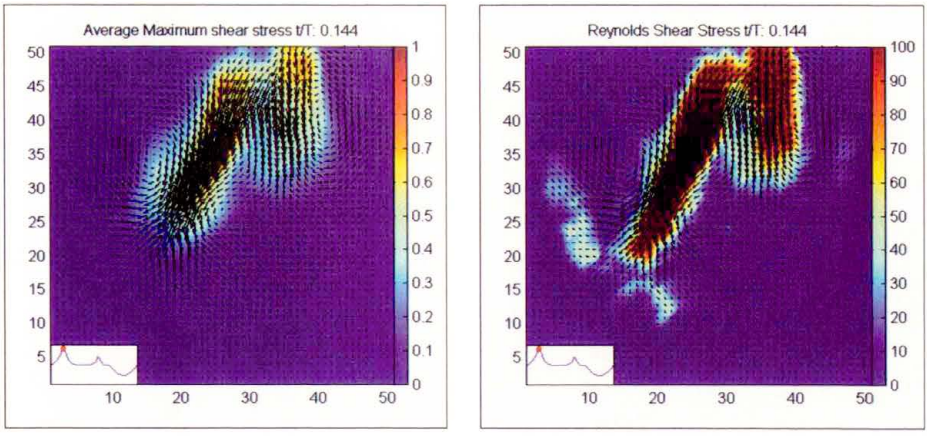

FIGURE 30. Phase averaged maximum viscous (on the left) and turbulent (on the right) shear stresses at one phase of the cycle (indicated by the red dots).

6. Simulation of Aortic Valves

Two main examples will be given of aortic flows downstream aortic valves; the first concerns with the Sheffield type mock-loop developed at ISS [7, 11] and the second with the Aachen unsteady pulse duplicator.

6.1. Sheffield Mock-Loop (ISS)

The experimental set-up of this experiment is given in Fig. 31 (refer to Sec. 2 for the figure and description of the mock-loop); in the first part of the figure a detailed view of the measurement region (aortic root) with position of the valve (bileaflet) and of the Valsalva sinuses is given (it is a pyrex replica of the real geometry). In the second part of the figure, the bileaflet valve is shown, while in the third part of the figure the control curve obtained for the flow rate is presented (beat rate equal to 70 Hz, flow rate equal to 1 l/min). In comparison to results on the ventricle presented in the previous section, the opening phase for the aortic valve is the systole while closing phase takes place in diastole. The working fluid is a water-glycerine (33%) mixture in Reynolds number (equal to 3200) and Womersley number (equal to about 10) similarities.

The measurements have been performed by means of a high-speed camera (the same used in Sec. 5) computing particle displacements by means of PTV [17].

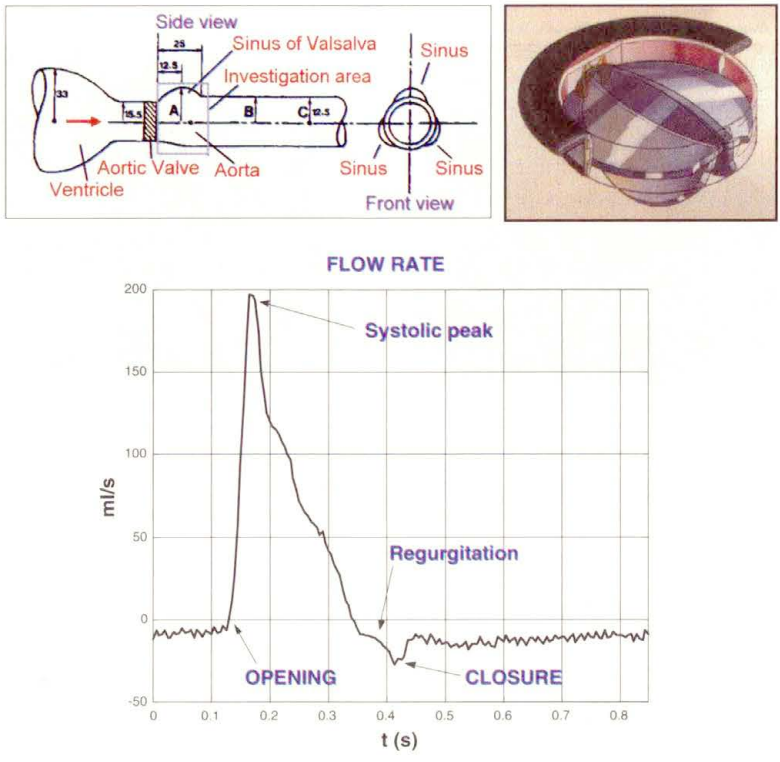

FIGURE 31. The experimental set-up for the aortic valve with Sheffield mock-loop (ISS) configuration; detail of the aortic root (top left), of the aortic bileaflet valve (top right) and of the flow rate during the cycle (bottom).

Some of the results obtained for the phase averaged fields are presented in Fig. 32 at the different phases; at the opening of the aortic valve (the phase is indicated by a red dot on the side of each figure), two jets start to develop directed towards the walls of the aortic root (the wake of the leaflet at the centerline partially obstructs the flow). As the valve opens the two leaflets generates three jets which fill all the flow field (second figure taken at the systolic peak). Immediately after the systolic peak (third figure), a recirculation starts into the Valsalva sinus on the right part of the investigated field; the main flow moves towards the left part of the field. After the closure of the valve (fourth figure) there is a clear backflow indicating some regurgitation; at this phase, the vortex in the Valsalva sinus changes sign.

As already stated, the interest in using PTV rather than PIV is in the possibility of deriving Lagrangian statistics, i.e. statistics of particles along

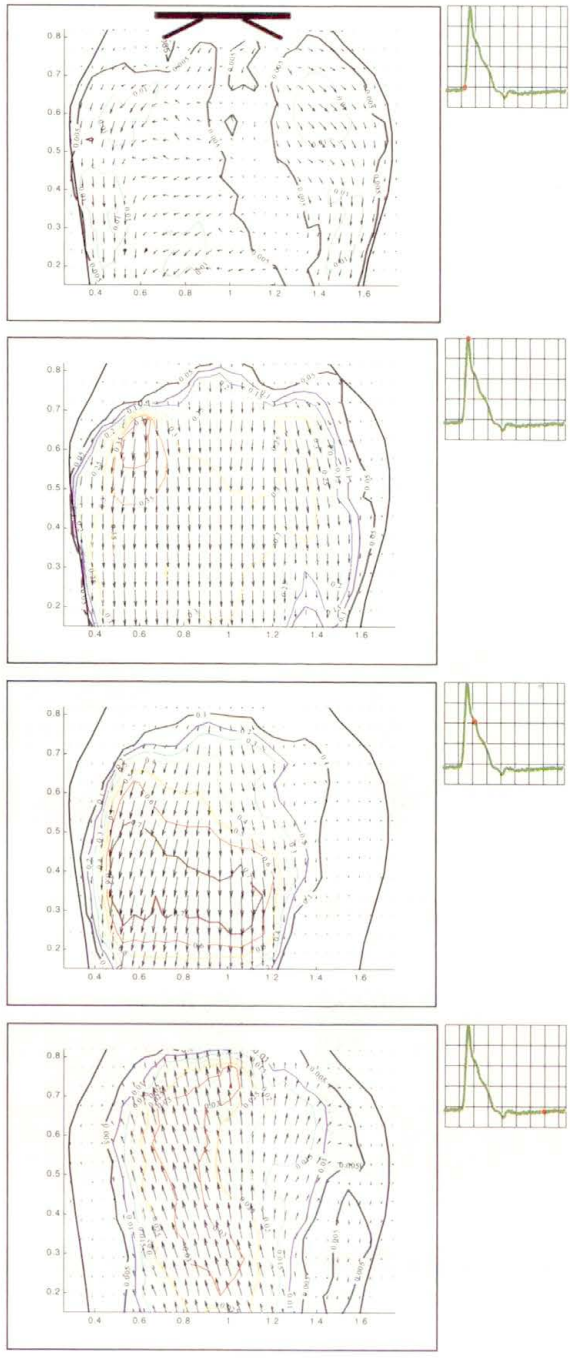

FIGURE 32. The phase averaged vector and axial velocity contour fields at four phases of the cycle (indicated by the red dots); the flow is from the top.

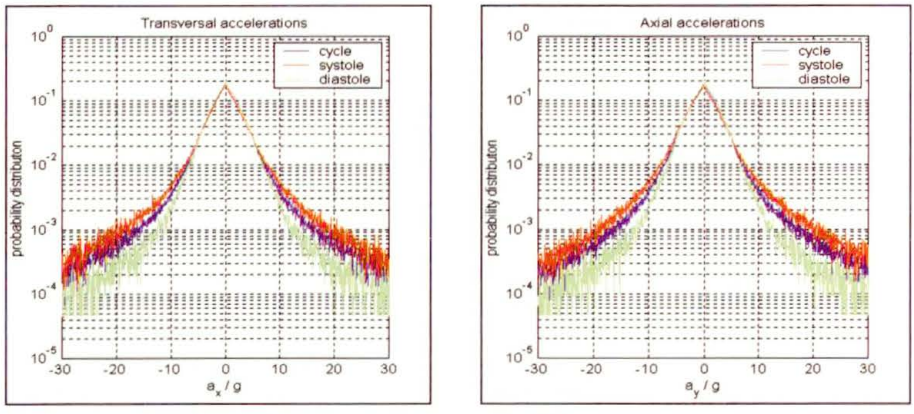

FIGURE 33. PDFs of transverse (on the left) and axial (on the right) accelerations from Lagrangian statistics during systole, diastole and the whole cardiac cycle.

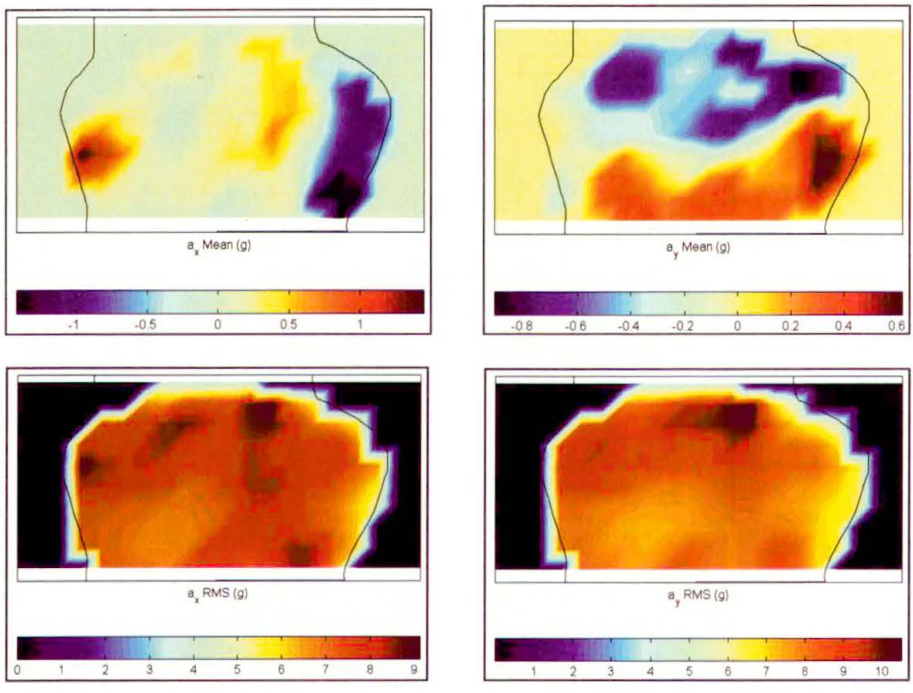

FIGURE 34. Transverse (on the left) and axial (on the right) accelerations from Lagrangian statistics during systole; average accelerations (at the top) and RMS of accelerations (at the bottom).

their trajectory. This is the most significant part which could allow to evaluate the accelerations, forces and stresses on each single blood cell. With this goal in mind, particle accelerations have been computed from the measured particle velocities along trajectories; in Fig. 33, the probability density functions (PDF) of transverse (indicated by a_x) and axial (indicated by a_y) accelerations all over the aortic root are evaluated. They are computed for the whole cycle (in blue) and separately for the systole (red) and diastole (green). It is observed that accelerations during systole are usually larger than those during diastole (both transverse and axial); moreover, axial and transverse accelerations are of the same order of magnitude (the average RMS value is about $3g$, where g is the gravity acceleration). Lastly, there are a few, but finite number, of particles experiencing accelerations larger than $20g$ (in absolute value).

The spatial distribution of the determined acceleration is given in Figs. 34 (systole) and 35 (diastole); in these figures, the average and RMS values of

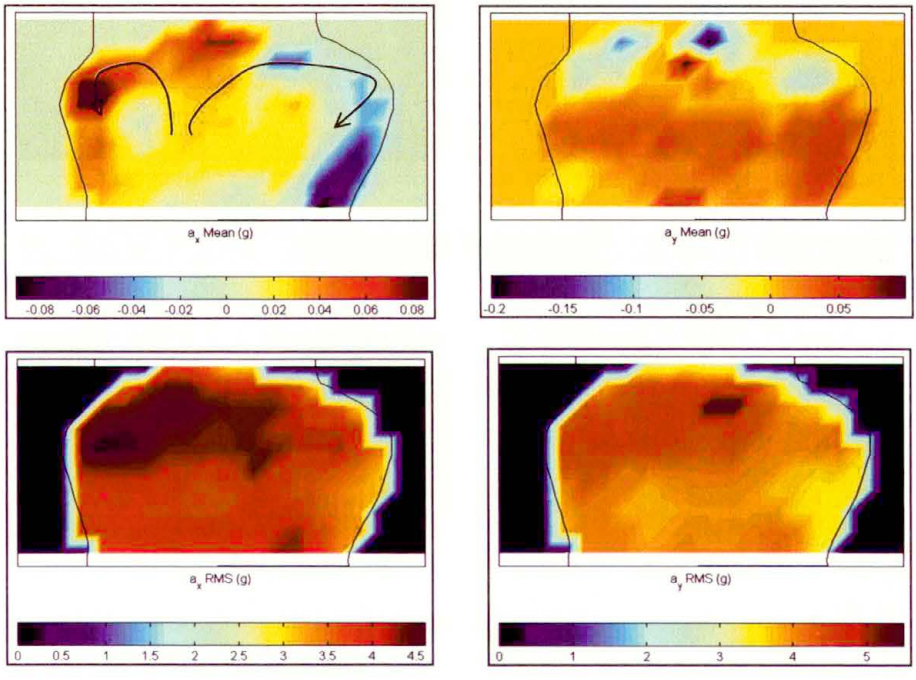

FIGURE 35. Transverse (on the left) and axial (on the right) accelerations from Lagrangian statistics during diastole; average accelerations (at the top) and RMS of accelerations (at the bottom).

the accelerations have been reported. During systole, the mean value of the transverse acceleration (first plot in Fig. 34) shows that the highest values are limited to the edge of recirculation regions and close to the jet reattachment points on the wall. The mean axial accelerations (second plot in Fig. 34), are negative (deceleration) at the expanding part of the root and positive in the contracting part. The RMS values for both transverse and axial accelerations (third and fourth plots in Fig. 34), are distributed much more uniformly than the mean.

The values are larger than the mean; the highest are obtained immediately downstream of the valve, indicating that inertial forces on blood cells are significant in this region.

During diastole, the mean value of the transverse acceleration (first plot in Fig. 35) shows that the highest values are observed close to the aortic

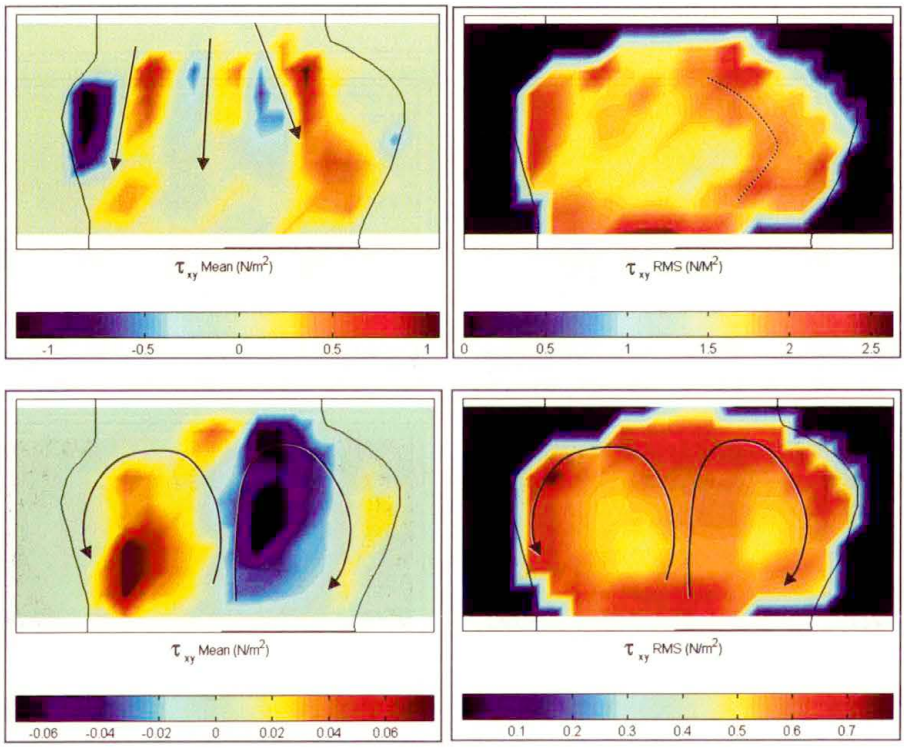

FIGURE 36. Viscous shear stress, average (on the left) and RMS (on the right) values from Lagrangian statistics during systole (at the top) and diastole (at the bottom).

root walls and at the top of the recirculation regions due to regurgitation (indicated by arrows). The mean axial accelerations (second plot in Fig. 35), due to the inverse flow in comparison to systole, are positive at the expanding part of the root and negative in the contracting part. All the mean values are lower than those during systole. Also during diastole the RMS values for both transverse and axial accelerations (third and fourth plots in Fig. 35), are distributed much more uniformly and with larger values in comparison to the mean. Even in this case the maxima are located close to the valve section. The RMS values are of the same order of magnitude than those during systole, thus indicating the relevance of measurements in the aortic root during the diastolic phase also.

Viscous stresses have been calculated from the data; in Fig. 36, the results for the mean and RMS values during systole and diastole are given. During systole (first two plots) the mean value indicates a three jet configuration, while RMS is maximum at the boundaries and in the recirculation region. During diastole (two plots at the bottom), the structure of a single regurgitant jet is depicted (lower mean values in comparison to systole); RMS values are of the same order of magnitude than during systole.

6.2. Aachen Mock-Loop

The experimental set-up is shown in Fig. 37 (refer to Sec. 2 for the figure and description of the mock-loop); in the first part of the figure a plot of obtained aortic, ventricular and atrial pressure curves is presented. As already stated in Sec. 2, it is quite complicated to set-up properly the circuit to obtain such curves, but the result is very similar to physiological ones. In the second part of the figure, the aortic pressure (which is the most critical one to control) is presented for three different measurements; as can be observed, once the circuit is properly set-up the variations from cycle to cycle are quite small. In the third part of the figure the flow rate downstream the aortic root is given (beat rate equal to 70 Hz, flow rate equal to 5 l/min). The working fluid is a water-glycerine (35%) mixture in Reynolds number (equal to 8000) and Womersley number (equal to about 10) similarities.

The measurements have been performed by means of a commercial cross-correlation PIV system (manufactured by LaVision Gmbh). A huge amount of data has been recorded and elaborated; only examples will be given in the following.

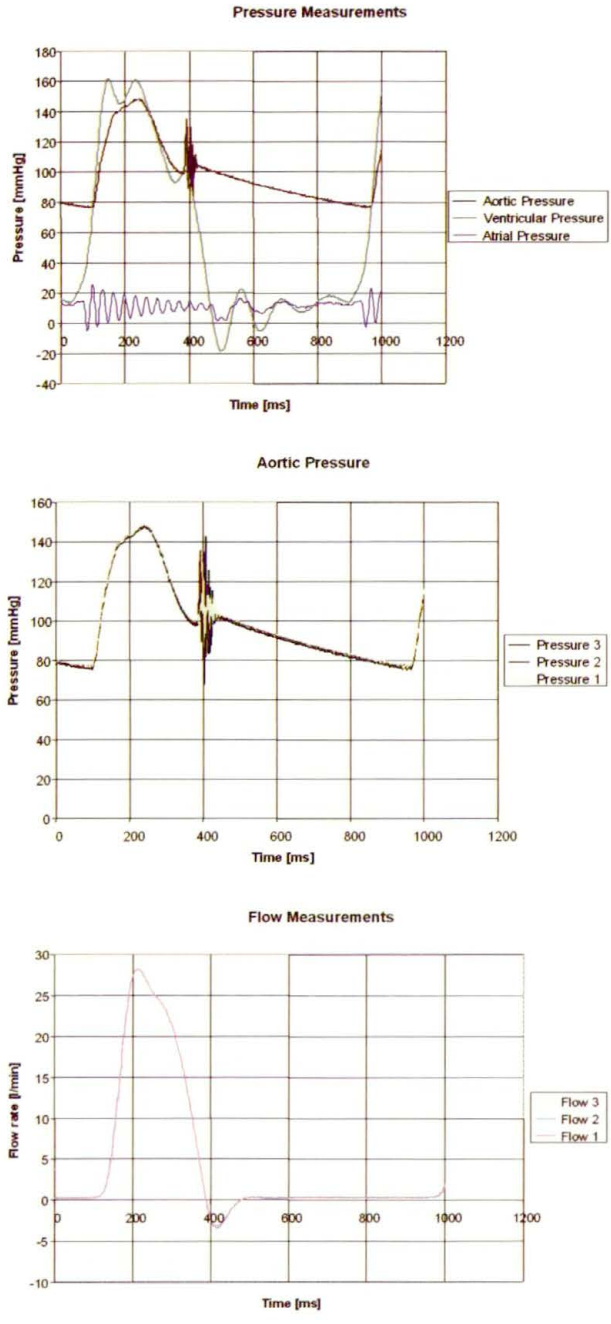

FIGURE 37. The experimental pressures (at the top), aortic pressure variations over three cycles (at the centre) and flow rate (at the bottom) for the aortic valve with Aachen mock-loop configuration.

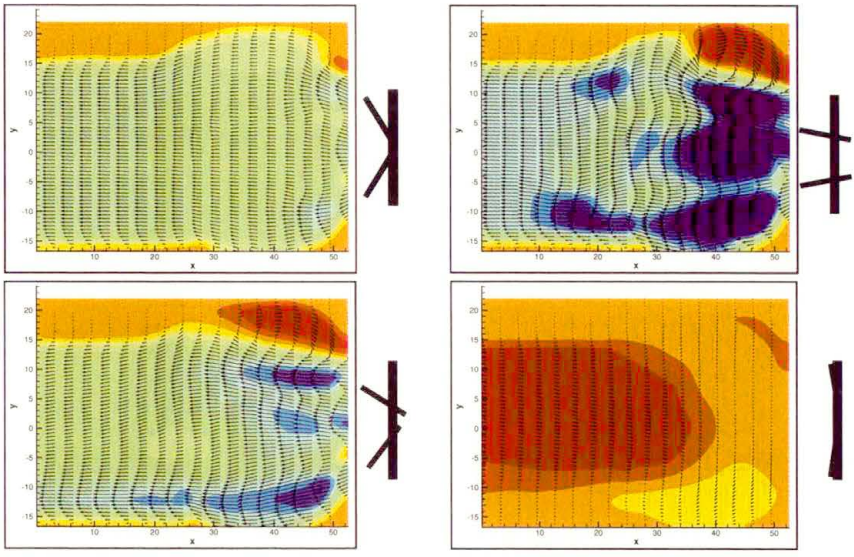

FIGURE 38. Phase averaged vector and axial velocity contour fields at four phases of the cycle (valve leaflet positions are indicated on the right of each plot); the flow is from the right.

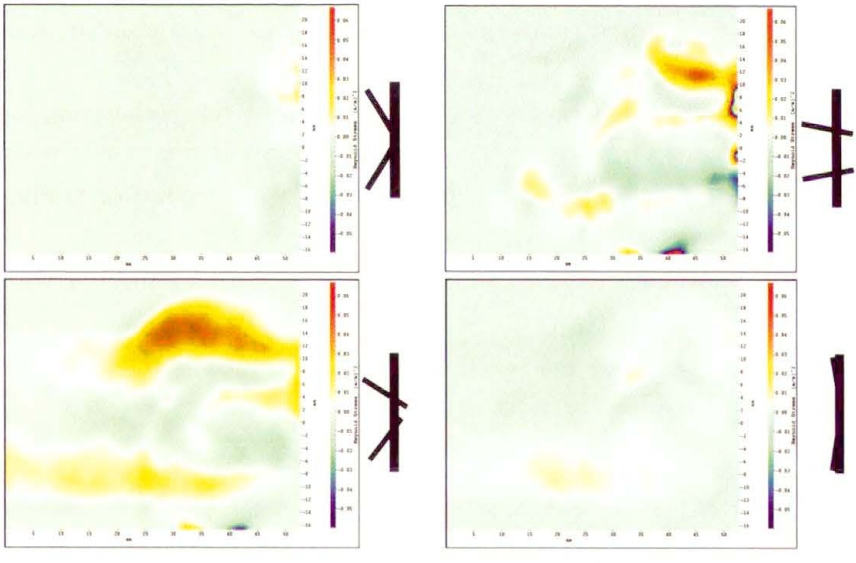

FIGURE 39. Phase averaged Reynolds turbulent stress fields at four phases of the cycle (valve leaflet positions are indicated on the right of each plot); the flow is from the right.

In Fig. 38, vector and horizontal velocity plots are given at four different phases. The valve bileaflet positions are also indicated on the left of the figures. The flow starts to move immediately after valve opening (first figure); then a three jets condition develops (second figure) as also reported in previous measurements. In the Valsalva sinus (at the top right corner), a recirculation region is observed which enlarges up to the phase in which valve leaflets start to close (third figure); at this phase, the three jets are still observed although attenuated. After valve closure (fourth figure), the backflow (regurgitation) takes place all over the field (except in the portion of the Valsalva sinus at the bottom right corner).

Higher-order statistics can be evaluated; as an example, the Reynolds turbulent stresses are presented in Fig. 39. The highest values are found at the upper Valsalva sinus (which is the only one completely investigated on the measurement plane) in a region which enlarges during the cycle. High values are also found at the jet boundaries especially at the bottom part.

7. Remarks and Future Developments

Remarks and conclusions will be given for each experiments. For the pulsed jet configuration (Sec. 4):

- optimal design and control of mock-loops is a crucial point in artificial valve testing;
- strong differences in the flow field are observed when changing forcing signal shape and flow rate, i.e. scaling is not allowed (velocity profiles);
- depending on flow rate and signal shape, concentrated or trailing jet structures in the wake of the main vortex ring are observed;
- these is evidence of an interaction between vortex ring and vorticity from previous vortex rings (at previous cardiac cycle);
- a preliminary statistical analysis for determining number of samples and type of statistics is required.

For the left ventricle silicone model (Sec. 5):

- average and turbulent kinetic energy have to be measured for proper heart valve evaluation;
- turbulent and viscous maximum shear-stresses are needed to point out the phenomena that more likely cause damage to blood-cells;
- the turbulent contributions cannot be neglected and seldom are the most relevant even at quite small Reynolds numbers;

- inertial forces on blood cells have to be measured from accelerations (i.e. from Lagrangian measurements).

For the Sheffield type mock-loop for aortic valve testing (Sec. 6.1):

- the fluid-mechanics phenomena in the aortic root as at least as complicated as those in the ventricle;
- three jet configuration during systole and regurgitation during diastole are derived;
- accelerations of fluid particle are significant and on average larger than those in the ventricle;
- it is important to evaluate average and RMS accelerations especially in recirculation regions and close to the valve;
- the comparison between mean shear stress and RMS values points out that the former permit the comprehension of the structure of the mean flow but underestimates the amplitude of the viscous forces on blood cells.

For the Aachen type mock-loop for aortic valve testing (Sec. 6.2):

- the set-up of a complex mock-loop for systemic circulation and prosthetic heart valve testing is not simple; once obtained it is stable;
- for the two-leaflets valve, the three jets configuration is visible independently on the employed mock-loop;
- regurgitation is also present on this mock-loop;
- large recirculation in the Valsalva sinus are observed leading to high RMS and Reynolds stress (due to vortex oscillations);
- there is a factor larger than 10 between velocities and second-order statistics determined at systolic peak and those in diastole.

The following points can be established as relevant for future investigations in the field of heart valve experimental testing:

- establish as much as possible procedures and apparatus (circuit, geometry, forcing, fluid, sampling) needed for proper valve testing;
- perform effective 3D experiments and numerics;
- evaluate accelerations and forces in a frame moving with the fluid particles;
- attain much higher spatial and temporal resolutions in experiments;

- perform simultaneous measurements of velocity, pressure and temperature fields.

Acknowledgements

Many of the results presented in this paper have been obtained within the framework of European Project IST 2002 37548 SMART-PIV (Development of an interactive integrated PIV system based on miniaturized optical sensor technology for implantable biomedical device design); all partners are acknowledged. The author wish to thank Dr. M. Falchi and Prof. G. Querzoli for the help in setting up the experiments and performing the measurements. Many thanks also to Prof. Z. Del Prete for setting up the driving motor for the pulsed jet apparatus, to Prof. A. Cenedese for providing the results on the left ventricle and to Dr. M. Grigioni for the helpful discussions and comments on the ISS data.

References

1. C.T. LEONDES, *Biomechanical Systems: Techniques & Applications*, Vol. II, Cardiovascular Techniques, `http://www.engnetbase.com/ejournals/books/`, 2004.

2. H. REUL, N. TALUKDER, and W. MULLER, *Fluid mechanics of the natural mitral valve*, Journal of Biomechanics, **14**:361–372, 1981.

3. H. REUL, J. VAN SON, U. STEINSEIFER, B. SCHMITZ, A. SCHMIDT, C. SCHMITZ, and G. RAU, *In vitro comparison of bileaflet aortic heart valve prothesis*, Journal of Cardiovascular Surgery, **106**:412–420, 1993.

4. M. GRIGIONI, C. DANIELE, G. D'AVENIO, and V. BARBARO, *A discussion on the threshold limit for hemolysis related to Reynolds shear stress*, Journal of Biomechanics, **32**:1107–1112, 1999.

5. Y.C. FUNG, *Biodynamics: circulation*, Springer-Verlag, 1997.

6. T.J.PEDLEY, *The fluid mechanics of large blood vessels*, Cambridge University Press, 1980.

7. A. BALDUCCI, M. GRIGIONI, G. QUERZOLI, G.P. ROMANO, C. DANIELE, and G. D'AVENIO, *PIV and PTV measurements downstream an artificial heart valve*, Experiments in Fluids, **36**(1):204–213, 2004.

8. A. CENEDESE, Z. DEL PRETE, M. MIOZZI, and G. QUERZOLI, *A laboratory investigation of the flow in the left ventricle of a human heart with prosthetic, tilting disk valves*, Experiments in Fluids, Online First, 2005.

9. M. FALCHI, Z. DEL PRETE, B. WIENEKE, G. QUERZOLI, and G.P.ROMANO, *The flow field at the outlet of a pulsed jet under different periodic signals*, Euromech Colloquium 456, Experimental and computational Biofluid Mechanics, Aachen, Germany, 2004.

10. A. CENEDESE, Z. DEL PRETE, M. MIOZZI, and G. QUERZOLI, *Investigations of the blood flow inside the left ventricle of the heart*, Euromech Colloquium 456, Experimental and computational Biofluid Mechanics, Aachen, Germany, 2004.

11. A. BALDUCCI, M. GRIGIONI, G. QUERZOLI, and G.P.ROMANO, *Measurements of forces on blood cells downstream an artificial aortic valve*, PIVNet2 Workshop on PIV in Biomedical Flows, Aachen, 2003.

12. M. FALCHI and G.P. ROMANO, *Experimental study on vortex rings dynamics in a pulsed jet using Particle Image Velocimetry*, Proceedings of 4^{th} International Symposium on Turbulence and Shear Flow Phenomena, Williamsburg, USA, 2005.

13. M. FALCHI, G.QUERZOLI, and G.P. ROMANO, *Investigation of a pulsed jet by means of Robust Image Velocimetry*, Proceedings of 6^{th} International Symposium on Particle Image Velocimetry, Pasadena, USA, 2005.

14. R.J.ADRIAN, *Particle Image Velocimetry for experimental fluid mechanics*, Annual Review of Fluid Mechanics, **23**: 261–304, 1991.

15. M. STANISLAS, J. KOMPENHANS, and J. WESTERWEEL, *Particle Image Velocimetry: Progress Towards Industrial Application*, Springer-Verlag, 2000.

16. M. GHARIB, E. RAMBOD, and K. SHARIFF, *A universal time scale for vortex ring formation, Journal of Fluid Mechanics*, **360**: 121–140, 1998.

17. A. CENEDESE and G. QUERZOLI, *Particle tracking velocimetry: measuring in the Lagrangian reference frame*, Von Karman Lecture Series 2000-2001, Von Karman Institute, Bruxelles, Belgium, 2000.